minerals

MDPI

Article

Characterization of Kinetics-Controlled Morphologies in the Growth of Silver Crystals from a Primary Lead Melt

Steven King [1,2], Dillon Rajoo [1], Alexander Norori-McCormac [1] and Alberto Striolo [1,3,*]

[1] Department of Chemical Engineering, University College London, Torrington Place, London WC1E 7JE, UK; steven.king1@glencore.com.au (S.K.); a.norori-mccormac@ucl.ac.uk (A.N.-M.)
[2] Britannia Refined Metals, Botany Rd Northfleet, Kent DA11 9BG, UK
[3] School of Sustainable Chemical, Biological and Materials Engineering, University of Oklahoma, 100 East Boyd St, Norman, OK 73019, USA
* Correspondence: astriolo@ou.edu

Abstract: Silver, a precious metal, can be recovered as a by-product of the processing of non-ferrous metals such as lead. In this work, silver crystals grown from the controlled cooling of a 10% silver–90% lead melt have been examined to quantify crystal morphologies developed under industrial conditions. X-ray tomography (XCT) is adapted to quantify the size and morphology of silver crystal structures grown from the Ag-Pb melt. The examination utilized high X-ray energies and small sample sizes to mitigate attenuation and enhance image quality. Examination of single crystal dendrites under high magnification demonstrates that silver crystals, even those grown under commercial conditions, yield a Face-Centered Cubic (FCC) crystalline lattice, which could be important for the practical extension of this work to the commercial production of Ag nano-crystals and crystalline supra-molecular structures. The crystals observed are composed of multiple twinned euhedral grains in a variety of dendritic to acicular arrangements, yielding a substantial heterogeneity of crystalline forms. XCT data were used to generate size and shape descriptors for the individual crystals. The results were compared to an equivalent set of descriptors generated from laser sizing examination of a sample of unconsolidated crystals from the same experimental run. The correspondence to within 9% of the crystal equivalent diameters determined independently by the XCT and laser sizing demonstrates a favorable outcome in particle sizing as achieved by visual inspection of XCT results. XCT examination of crystal assemblages identifies small octahedral crystals and larger triangular platelets. The structures expected for FCC crystals grown at thermodynamically controlled conditions are not observed in our systems, suggesting the possibility of the first crystal nuclei form at such conditions, but their growth transition to kinetically controlled mechanisms occurs as their size increases above a threshold cutoff. Based on literature observations, this size threshold is much smaller than the resolution of the XCT instrumentation employed herein. Our characterization data are in fact consistent with thermodynamics/kinetics—and then kinetics-controlled mechanisms—as the crystal size increases. This observation is important because the systems considered here are representative of commercial processes. As such, this work extends prior crystal growth concepts, which were explored in aqueous systems often probed by electrodeposition.

Keywords: crystal size distribution; X-ray tomography; laser sizing; twinned euhedral grains; commercial conditions

Citation: King, S.; Rajoo, D.; Norori-McCormac, A.; Striolo, A. Characterization of Kinetics-Controlled Morphologies in the Growth of Silver Crystals from a Primary Lead Melt. *Minerals* **2024**, *14*, 56. https://doi.org/10.3390/min14010056

Academic Editor: Rajesh Kumar Jyothi

Received: 31 October 2023
Revised: 16 December 2023
Accepted: 29 December 2023
Published: 1 January 2024

1. Introduction

Silver, an element useful because of its ductility, conductivity, low reactivity, and antibacterial properties [1–3], crystallizes within the cubic crystal system. In the natural environment, Ag is found in its native form as well as in the form of an accessory element associated within several silver compounds within larger ore bodies. Although Ag is known to form singular euhedral crystals [4,5], this is a rare occurrence; typically, where found in its native state, Ag forms elongated dendrites as well as other complex crystal structures.

There has been growing interest in the controlled synthesis and recovery of various silver crystal structures, as Ag nanotubes, dendrites, and other complex structures have unique optical, electronic, and magnetic properties, suggesting a range of applications in materials science and industrial processes [6]. A wealth of the literature quantifies the growth and assembly of Ag supra-molecular structures in a range of controlled aqueous, low-temperature environments [7–12]. Of particular interest to the present contribution is the examination of the electrodeposition of metallic Ag crystals [13]. At low over voltages, the {111} plane was found to be the dominant growth plane for Ag, Au, and Cu crystals; only increasing the overvoltage achieved growth on the {100} and {110} planes. More recently, the morphology and crystal structure of metal powders produced by electrolysis has been investigated [13]. In the case of Ag and other FCC metals (i.e., Pb and Cu), crystallization was predominantly orientated along the {111} plane; other planes such as {200}, {220}, and {311} became evident with increasing overvoltage. In fact, as the overvoltage was increased, fine needle-like dendrites were overtaken by cauliflower-like morphologies. Representative results [13] are reported in Figure 1. These images will prove useful as a comparison for the results obtained in the present work. Indeed, it should be stressed that the results reported previously [13,14] clearly support {111} as the preferred growth plane at moderate driving forces, as the degree of undercooling during crystallization from molten systems has an equivalent role to overvoltage in electrodeposition and supersaturation in vapor systems. The crystallization process results in the {111} plane as that which dominates the surface of the final crystal structure.

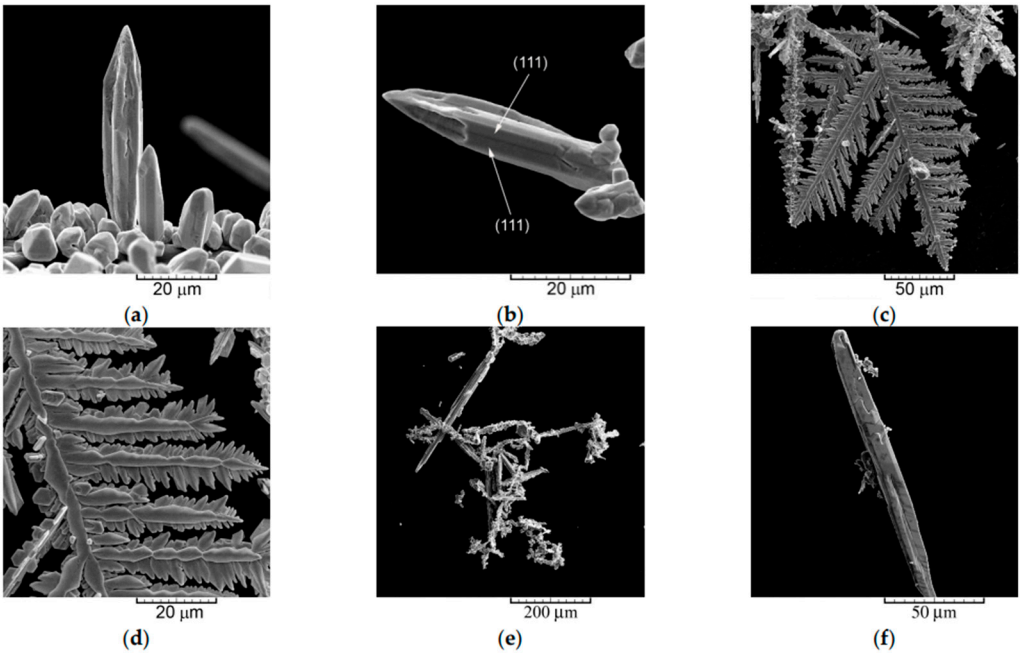

Figure 1. Morphologies of Ag powder particles produced by electrodeposition from a nitrate electrolyte (0.1 M $AgNO_3$, 2.0 M $NaNO_3$) at over potentials of (**a**,**b**) η = 90 mV and (**c**,**d**) η = 150 mV, and at a current density of (**e**,**f**) J = 14.4 mA cm^{-2}. Figure reproduced with permission [14].

To rationalize the prior observations, it helps to remember that the relationship between surface energy and the preferred plane of growth is understood from the framework of the Bravais theory; the higher the surface energy of a surface (e.g., the smaller the reticular density of a surface), the faster will it grow normal to itself. Because the fastest growing surfaces soon disappear from the crystal, in the final crystal, only the surfaces with the slowest perpendicular growth persist. In Figure 2, we reproduce a schematic [15] to illustrate this accepted phenomenon. Within this theoretical framework, the results summarized above consistently identify the {111} crystallographic plane as the most favorable growth plane at mild conditions; it remains questionable whether these insights

can be extrapolated to conditions of commercial relevance for the metallurgical sector (e.g., high-temperature crystallization in the presence of cooling poly-metallic systems). The present manuscript explores this hypothesis, with the potential of identifying large-scale processes for manufacturing Ag crystals and crystal assemblies. The controlled growth of Ag crystals under commercial conditions is an inherently arduous prospect, as it involves managing controlled cooling in large batches at high temperatures and involves trying to characterize fine-scale morphologies in an opaque medium. Indeed, the sparse prior investigations on the subject have been limited to theoretical work in a narrow range of conditions [16,17].

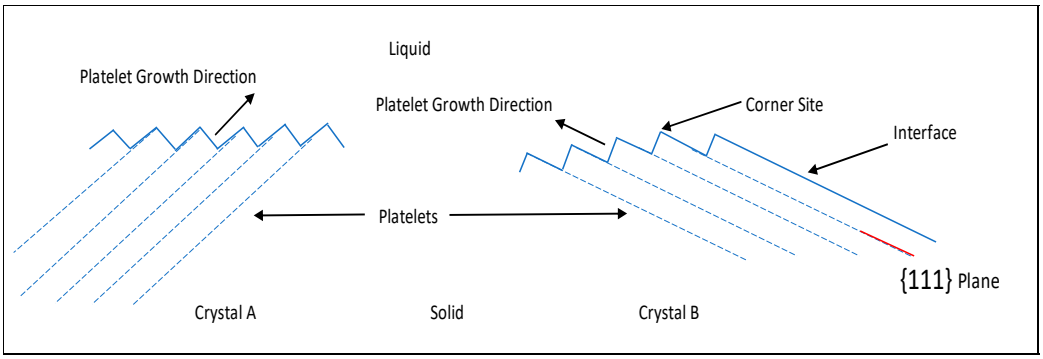

Figure 2. A trace of the solid–liquid interface on a section parallel to the axis of growth which represents the edgewise growth of platelets. Figure reproduced with permission [15].

To place the present contribution in a wider context, it helps recalling that the solidification of lead was examined [15] and the crystal growth noted was consistent with the Bravais theory. It was noted that the crystalizing interface between solid and liquid lead developed to present the {111} plane as the dominant expressed crystal surface. The solidification of Face-Centered Cubic (FCC) metals, which include lead and silver, was examined [18]; it was noted that the preferred direction for solidification in pure melts was normal to the {111} plane. Slight levels of impurities resulted in changes in the preferred direction of solidification, with alloy systems showing a {100} preferred orientation. It was further noted [15] that in Ag-Pb alloys with > 5 ppm Ag, the {100} orientation was preferred.

The latter result highlights the possible effect of impurities on crystal growth. In fact, the effects of impurities, as well as that of system conditions, on the resulting crystals have been studied by several groups. For example, conducting experiments at a high temperature [16] demonstrated that the crystal growth rate is affected by the rate of heat removal. The final morphology of the solid material produced was determined by a combination of crystal structure, rate of heat removal, degree of undercooling, composition, and impurity levels. A model was developed that considered the effect of volume change upon solidification (~4%) [16]. The model predicted preferred solidification structures consistent with those observed by earlier researchers [16], who identified a preferred {111} growth plane in pure lead systems, which transitioned to a {100} orientation as the impurity (Bi) levels increased. It was noted [19] that dendrites typically grow along the direction corresponding to the maximum in surface free energy. For FCC metals, such growth is generally in the {100} direction; however, in some Al alloys, dendrites can select other orientations, depending on several factors. For example, the influence of the cooling rate in defining the preferred growth direction has been noted in several metal systems. In the unidirectional cooling of Al-Si alloys, it was noted [20] that cooling produced dendrites that possessed {110} trunks, cut through by {111} twin planes. In further research [21], the effects of temperature and impurities on the preferred crystallographic orientation of silver and copper solidified in contact with a silica substrate were investigated. Both Ag and Cu present FCC structures. The {111} and the {100} planes were noted as the preferred orientations for pure silver (being the planes parallel to the silica substrate used in the experiment), and a shift to the {100} plane was observed for an alloy of Ag-Bi (500 ppm). At

temperatures of 98% of the melting point, the {100} plane became dominant. This is detailed in Figure 2, where the preferred growth direction normal to the {111} plane presents this plane as that which is expressed in the final crystal structure.

A range of imaging techniques have been used to qualitatively and quantitatively evaluate the crystals described above. At both micro- and nanoscales, scanning electron microscopy (SEM) enables the two-dimensional analysis of the structure as well as a chemical analysis of the composition; higher resolution X-ray computational microtomography (XCT) is occasionally used for nanoscale investigations of crystalline metallic structure [10,11]. It is noted that XCT offers the potential for three-dimensional structural investigations at micro- and nanoscales. However, the study of high-density metallic crystals and compounds with XCT is difficult due to the attenuation and absorption of X-rays, making it often impossible to visualize bulk structures. As a result, XCT has predominantly been used only in some specialized investigations, for example, to identify the presence of Ag within lower density mediums, particularly in biological applications [22,23]. To overcome these technical limitations, prior work by others concentrated on systems characterized by low Z–high contrast alloy pairs such as Al-Cu [24], probed in small samples [25]. Glass foams have been used to assist X-ray tomography [26]. For example, the growth of barite was observed within the voids of a silica matrix [27]. Other researchers [28] implemented microstructural tomography, which involves progressive grinding/micro toning down through a specimen, with the subsequent computational reconstruction of the 3D structure. It should be recognized that this technique leads to the complete destruction of the specimen.

In this study, we extend the use of X-ray tomography to quantify the morphology and crystal habit of high-purity Ag crystals, grown under the controlled cooling of a lead–silver melt. The Ag-Pb system is chosen because of its commercial significance, as most of the silver produced in the world is generated through the refining of lead bullion, silver being a common associate with lead in mineral deposits [3]. The samples used herein were provided by Glencore AU and were all generated under controlled process conditions, which allow us to propose a relevant hypothesis for the growth mechanisms of Ag crystals from commercially relevant conditions. The composition of the Ag crystals is detailed in Table 1. In the molten systems used here, Ag was an accessory component of Pb bullion, which has been remelted and then cooled in a controlled manner. The resulting Ag crystals were passively recovered and then subjected to bulk and individual analysis.

Table 1. Impurity content of Ag crystals based on mass balance of cooling crystallization system used to produce the Ag crystals studied here. Other species indicated below include oxygen, bismuth, and other elements.

Species	Mass %
Ag	72.91
Zn	0.18
Pb	24.30
Cu	2.60
Other species	0.01
Sum	100.00

This work seeks to examine crystals grown in full-scale physical and thermal environments, with the understanding that the growth of crystals in a large-scale process environment could be fundamentally different compared to the lab-scale preparation of very small samples [24,25]. Via the selective removal of the lead phase while molten, X-ray tomography has been applied successfully to a high Z alloy pair. The original technique described in the Methods section, as applied to metal alloy systems, enables the fine-scale examination of individual crystals, without the influence that crystallization would introduce on a fine scale. Our work has enabled the examination of a complete crystal assembly as generated in a large-scale physical environment with an equivalent cooling experience. The recovery of unconsolidated crystals from the same experiment and their independent

characterization by alternative means allowed us to further validate the reliability of the X-ray tomography technique via a double-blind approach. The results show excellent agreement.

The remainder of this manuscript is organized as follows: the experimental procedure implemented to produce the Ag crystals is first briefly summarized, together with the methods followed for conducting the XCT experiments; then, the characterization of the samples as obtained by X-ray tomography is presented. In the Discussion, the X-ray tomography data are corroborated by independent particle size distribution analysis and interpreted within the perspective of identifying the prevalent growth mechanisms (thermodynamically vs. kinetically limited) for the industrial systems considered. We conclude by summarizing our main results and their significance for the control of Ag crystal morphology in systems of commercial relevance.

2. Experimental Methods

2.1. Synthesis of the Ag Crystals from Ag-Pb Molten Alloys

Silver-dominated crystalline samples were produced from a molten 10% silver–90% lead alloy. The alloy was molten and then cooled from 500 °C to 400 °C. The cooling rate was approximately 1.85 °C per minute. The commencement of silver crystals' formation was observed at 474 °C, with 50% of the original silver content being crystalized out once the temperature reached 400 °C. Pb remained in a molten state in the entire temperature range sampled during the process, as demonstrated by the phase diagram of Figure 3 [29].

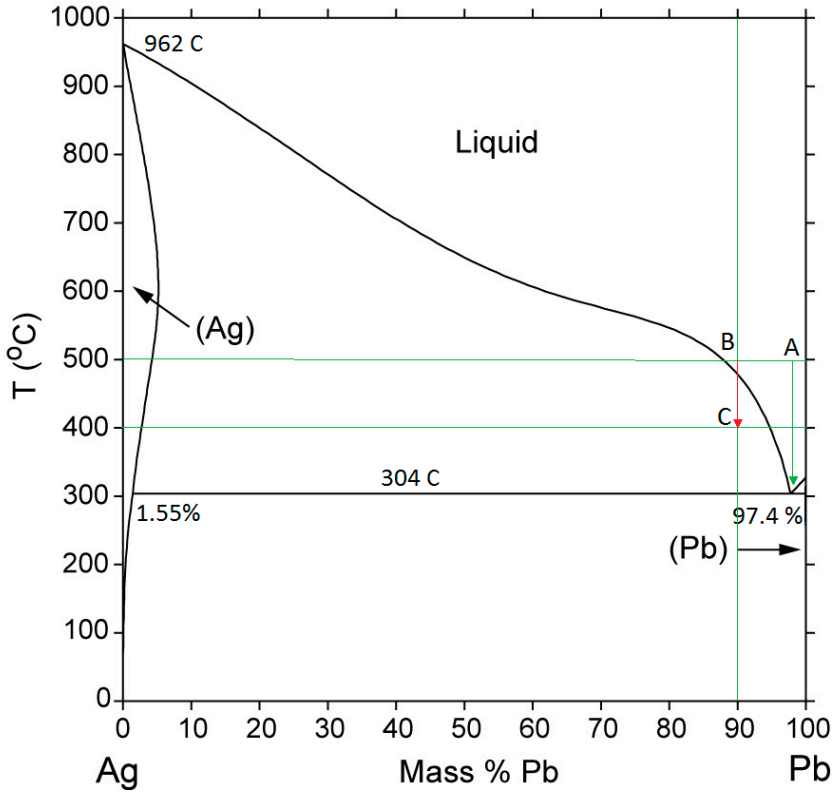

Figure 3. Ag-Pb phase diagram [29,30]. Point A details the eutectic composition at 2.6% *w*/*w* Ag. The red line from B to C shows the cooling of the Ag-Pb alloy conducted in this work, from an entirely molten state at 500 °C to a liquid–solid mixture at 400 °C.

The silver crystals, being of a lower density than liquid Pb, float to the surface of the melt and were recovered for subsequent examination by passive drainage of the liquid bullion. Cooling was interrupted at 400 °C to ensure the recovery of a sufficient silver crystal mass for subsequent XCT examination. This temperature enables an acceptable level of passive drainage of the liquid lead phase to be achieved, due to the low viscosity and

low surface tension of the molten Pb at this temperature. An example of the Ag-dominated crystalline samples produced and used for further characterization is provided in Figure 4.

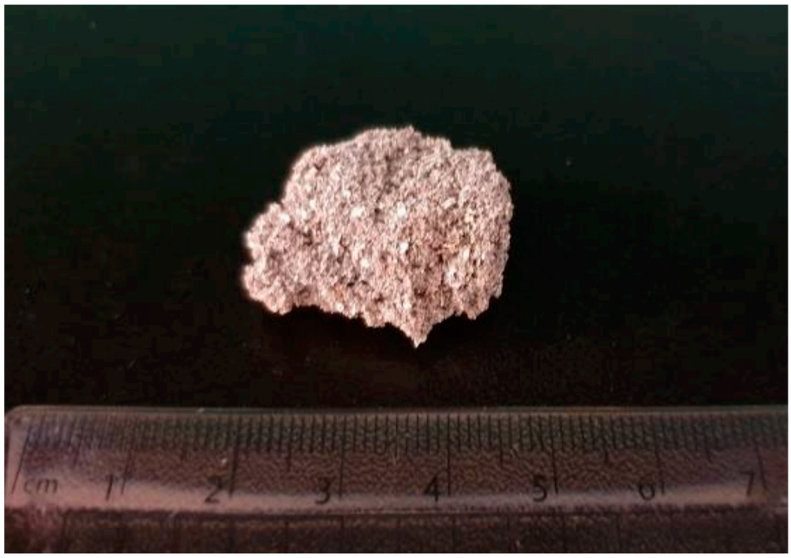

Figure 4. Optical image of a fragment of Ag crystalline mass produced for the present manuscript. The scale bar provides an estimate of the size of the Ag structure.

Crystal samples such as the one shown in Figure 4 were mechanically extracted to obtain cores to be scanned by XCT. A sample of ~5 mm^3 of crystals was separated out for bulk analysis, and a single crystal was extracted from the original sample for individual analysis of the crystal morphology and structure. The recovery of individual silver crystals for higher resolution imaging and to provide material for laser sizing work was accomplished by the agitation of consolidated samples, the fragile nature of the crystal assemblages enabling easy fragmentation into individual crystals. XCT was chosen to image the crystals in bulk and to image individual crystals to establish the overall characteristics of the silver crystal product, as well as investigate the structure of a single crystal under higher magnification, in terms of crystal habit and growth textures.

Unconsolidated silver crystals from the same batch were also used as part of the laser sizing and shape characterization work detailed in Section 2.3, to enable double-blind comparison of the results.

2.2. X-ray CT Characterization

The three-dimensional crystal morphologies of Ag aggregates were investigated using two X-ray imaging systems: the Nikon XT H 225 (Nikon XT H 225, Nikon Metrology, Tring, UK) and the Zeiss Xradia 520 Versa (Carl Zeiss X-ray Microscopy Inc., Pleasanton, CA, USA). The Nikon XT H 225 provides higher resolution and a larger field of view (FoV) and was used to image the morphologies of crystals in a bulk sample, whereas the Zeiss Xradia 520 Versa was used to image a single crystal in the micron size range.

For the bulk sample used in the Nikon XT H 225 instrument, a total of 1700 radiographs were acquired over a 360° sample rotation range, with an exposure time of 0.94 s per radiograph. The source-to-detector distance was 90 mm, with a 1 mm copper filter used for beam hardening. A voxel size of 5 µm was achieved, with the instrument operating at 225 kVp energy and a current of 70 µA. The scan was reconstructed in CT Pro 3D (Nikon Metrology, Tring, UK). The Nikon uses a Perkin Elmer 1620 flat panel detector plate and is not a microscope. For data captured by the Nikon XT H 225, segmentation was conducted through the selection tools in the segmentation editor in Avizo; segmentation was challenging in terms of defining individual crystals as there was no contrast between them. The crystals were manually marked with the brush filter in the xy, xz, and yz orientations in up to 30 slices of the data set, each assigned as a separate material number.

The watershed filter was then used to render the selected crystals in 3D, interpolating the identified region throughout the volume. Segmentation for the crystal scanned with the Zeiss Xradia 520 Versa was straightforward; one individual crystal was scanned, which could be selected and rendered as shown in the greyscale images (see Appendix D), and the results present high contrast with respect to the remainder of the volume, albeit some level of artifact is recognized (see Appendix D). The high-contrast region was selected using the segmentation editor and rendered in Avizo. No filters were used in the Versa scan.

Single Ag crystals were examined using the Zeiss Xradia 520 at both 4× and 40× levels of magnification. During imaging of the whole crystal at 4× magnification, a total of 1986 radiographs were acquired over a 360° sample rotation range with an exposure time of 15 seconds per radiograph. The source-to-detector distance of 52.9 mm provided a voxel resolution of 702 nm using the 4× objective magnification in binning 2 mode. For the 40× magnification, a total of 1001 radiographs were acquired over a 360° sample rotation range with an exposure time of 51 seconds per radiograph. The source-to-detector distance of 11.94 mm provided a voxel resolution of 365 nm using the 40× objective magnification in binning 2 mode.

In both cases, the Ag crystal was placed between the X-ray source and the 2k × 2k detector, and the instrument was operated at 160 kVp energy and a current of 63 µA. Both the 4× and 40× scans were reconstructed via the Zeiss XMReconstructor software package (Carl Zeiss X-ray Microscopy Inc., Pleasanton, CA, USA), which employs a filtered back-projection algorithm.

In all cases, the image volumes were subsequently segmented in the Avizo software package [31] (Avizo 2020.3, Thermo-Fisher Scientific, Mérignac Cedex, France). To obtain representative results, 24 individual crystals were examined using this software.

Several technological advancements compared to prior literature studies were implemented here to enable the X-ray characterization of the Ag-Pb samples:

- Optimized stirring: the Ag crystals produced during cooling showed a sensitive response to the stirring rpm and stirring type and position. Proprietary results led us to identify a stirrer type and rpm that maximized the crystal size.
- Vacuum sample impregnation: the as-solidified Ag crystal structure was found to be very fragile and difficult to handle for subsequent X-ray imaging. The preservation of the as-solidified Ag crystal structure was achieved by prompt lead drainage of the recovered crystal mass followed by impregnation with acrylic resin under vacuum to in-fill the open pore structure of the sample.

2.3. Particle Size Distribution via Dynamic Laser Imaging

In order to determine the particle size of silver crystals independently, three 50 g portions of unconsolidated silver crystals produced from the same test run as that used to generate the samples imaged via XCT were directed to RCPE (Research Centre Pharmaceutical Engineering) in Graz, Austria. These crystal samples were dispersed in a water carrier and the dynamic imaging of the suspended particle silhouettes was obtained by laser scanning.

The particle size and shapes were measured and quantified in terms of:

- Particle size (i.e., radius) distribution.
- Aspect ratio.
- Sphericity.
- Convexity.

These terms are defined in Appendices A and B.

2.4. Quantification of Impurities Content

The generation of the Ag crystals from a cooling lead–silver alloy in a commercial process will contain some impurities, which might have the potential to strongly influence crystal morphology in both aqueous and molten systems, according to the literature observations reviewed in the Introduction.

Bulk examination of the impurity content of the Ag crystal mass used in the present project is challenged by the amount of silver present, but a mass balance was conducted on the entire cooling crystallization kettle. Table 1 provides some estimates of the major impurity species present. These data are from assays performed on bath samples extracted from the molten system at temperatures above crystallization (e.g., point B in Figure 3).

In addition, an examination via scanning electron microscopy (SEM) was conducted in the coherent crystal samples to identify the major known species evidenced in the mass balance. The SEM concentration map for a previously imaged coherent crystal mass is shown in Figure 5. Despite the resolution limitations in the combined image (bottom panel), the image presents crystal facets free of copper, which appears concentrated on other planes. There appears to be less crystallographic correspondence for the distribution of lead, which is consistent with this element having been retained as the last component to solidify rather than crystallographic preference, as qualitatively confirmed by Micro-CT scans and by a power spectrum (see Appendix C).

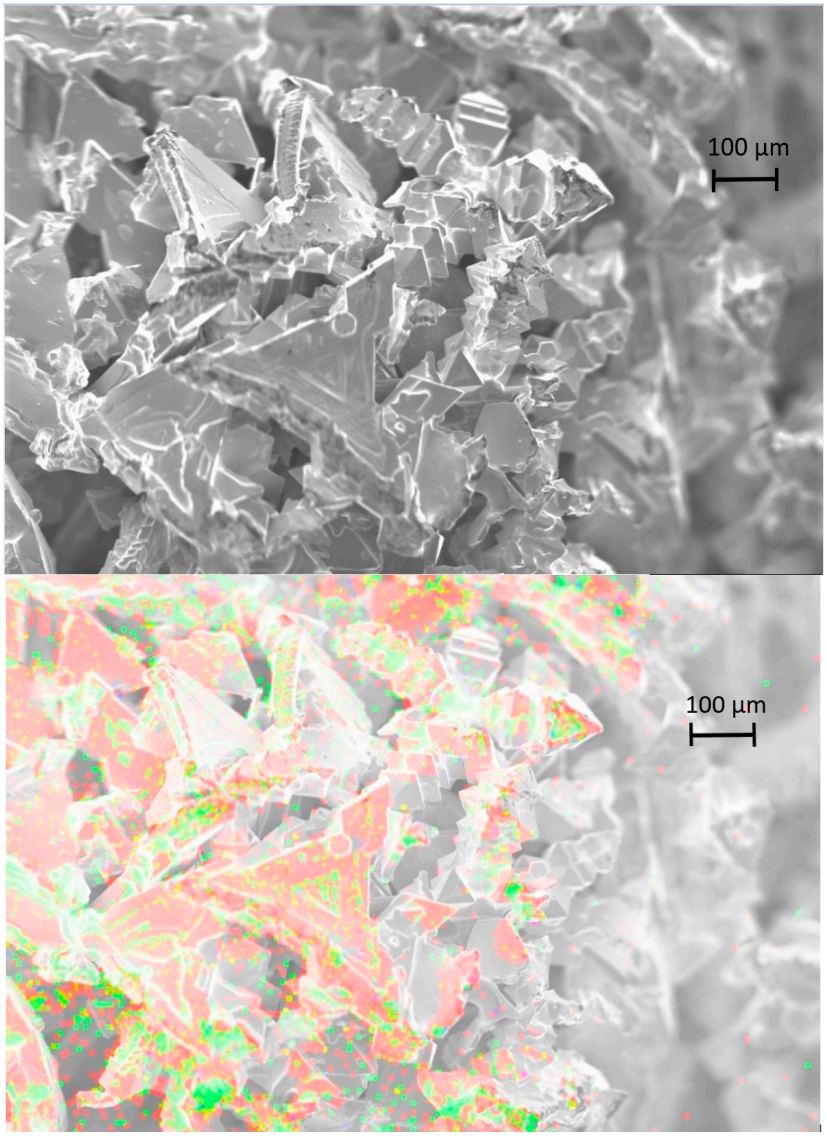

Figure 5. SEM image of coherent Ag crystal assemblage. Top: Black and white image illustrating the different crystal structures. Bottom: The red color areas indicate Ag, the green Pb, and the yellow Cu. These results are qualitative, as the equipment was not able to be calibrated for quantitative analysis of the sample.

3. Results

3.1. Image of Crystals under Reflected Light Microscopy

As can be seen in Figure 6, a range of complex crystal structures are present within the Ag aggregate produced from molten Ag-Pb system. Visual characterization of the results in Figure 6 suggests the presence of octagonal crystal grains with triangular faces. The crystals present well-defined facets, are subhedral to euhedral in form, and display a variety of sizes. The crystals are arranged in dendrites with complex forms and arrangements; grains of various sizes seem to have intergrown to yield the crystals. The individual grains within the crystal structures range from below 100 µm in size up to ~200 µm along their longest axis, whilst larger structures of up to 1000 µm along the longest axis can be observed. In comparing these crystals to those presented in Figure 1 (which are from the literature and obtained via electrodeposition from aqueous systems), it appears that crystal contact, damage, and intergrowth are far more prevalent in the present sample than in the crystals produced by electrodeposition, probably because of the commercial process conditions. The electrodeposited crystals used in Figure 1 have been produced in a much lower shear environment than those crystalized herein, which were produced from well-stirred molten material. The consequences expected from the high shear environment include crystal damage and regrowth, although the high shear allows for more efficient heat removal and management of processing times at the industrial scale.

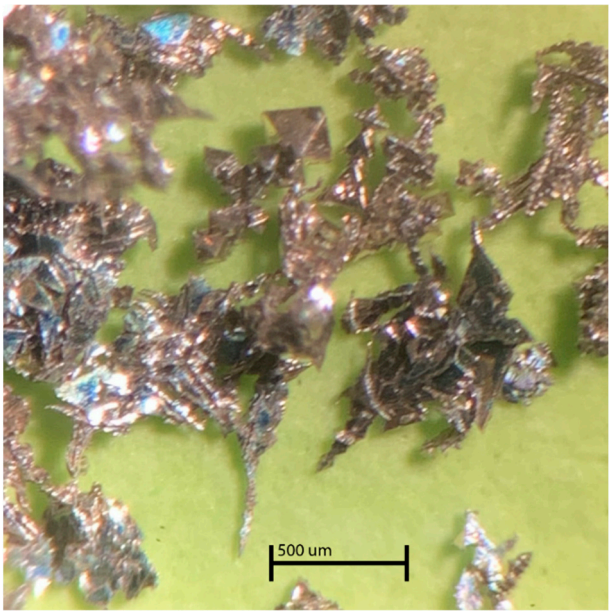

Figure 6. Reflected light microscopic image of disaggregated silver crystals from the sample shown in Figure 4. Note the range of crystal morphologies present.

Analysis of the results suggests that the driving forces for crystal morphologies appear to be similar in the aqueous and molten metal cases. If the aqueous crystallization were to be conducted in a high-shear stirred environment, the crystal produced would be expected to be far less pristine than those encountered in Figure 1 and much closer to those observed in our experimental work.

3.2. Bulk Crystal Mass Analyzed via XCT

A fragment extracted from the Ag aggregate shown in Figure 4 was scanned in the Nikon XT H 225 to quantify the 3D structure of a bulk Ag crystal at the individual crystals' domain. The fragment was ~25 mm × 10 mm in size. The XCT experiments yielded the reconstructed images shown in Figure 7 as the results.

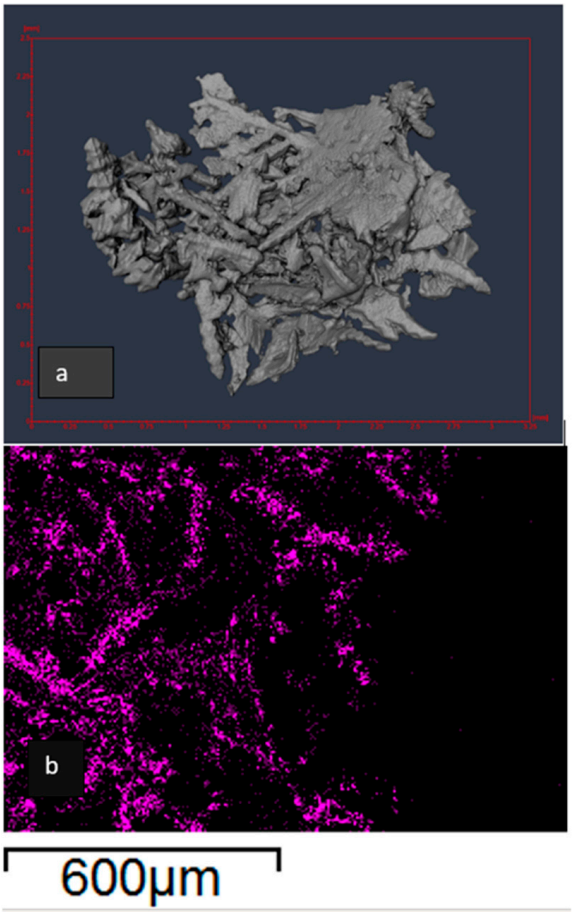

Figure 7. (**a**) An overall profile of the sample scanned using XCT, demonstrating the array of crystal forms, dominated by acicular, needle-like forms on the left-hand side of the image within a porous matrix, and the right-hand side being welded together, probably with excess lead. The silver crystals are interpreted to be an aggregate of smaller crystals of different orientations and not a single crystal. The presence of lead is evidenced in SEM imaging presented in (**b**), with the section of the crystal with lead being indicated in purple. Because Pb comprises 25% of the sample mass and because it is the last component to solidify, incomplete removal during preparation leaves solid lead as a binding agent.

The bulk sample, as shown in Figure 7a, presents a range of different crystal structures, which are clear on the left-hand side of the image. The structures are overall elongated, acicular in form, and extend up to 500 µm in length. There are repeating textural patterns evident within the crystal structures and between the individual distinct structures. The crystal structures are bound together within a lead-dominated matrix that obscures the silver crystals structures, which can be seen as black areas on the figure. This is a consequence of the crystallization out of a molten lead alloy and the incomplete removal of molten lead during sample preparation (Figure 7b). Our observations suggest that the lead matrix does not affect the crystal morphology. As can be seen in Figure 7a, and highlighted in Figure 8, the crystal structures observed in the bulk of the Ag sample can yield complex dendritic patterns and present themselves in a range of chain lengths. The entanglement of long silver crystals formed during crystallization and their binding due to incomplete removal of molten lead during sample preparation are the mechanisms of agglomeration.

The crystals within the Ag sample are formed of several individual grains with some degree of penetration evident, resulting in the acicular forms visible in Figure 8a. The grains comprising the larger structures are not always uniform in size throughout the structure. The penetration of the crystals within the associated structures appears to take several forms, with longer chains of grains present as well as individual crystals or

penetrative twinning of two or three grains in different orientations, which are clearly visible in Figure 8a,c. There is evidence of a more complex herringbone-like twinning structure in Figure 8b,d, with a central spine and numerous branches of silver grains at an acute angle to the spine. Although a repetitive pattern of grains within these crystalline structures is evident, it is not completely clear within scans at the resolution provided by the images presented so far. Higher resolution scans are required to fully appreciate the nature of the contact between the crystals, as well as the textures of the grains and their facets. Such analysis is attempted on single Ag crystals in what follows.

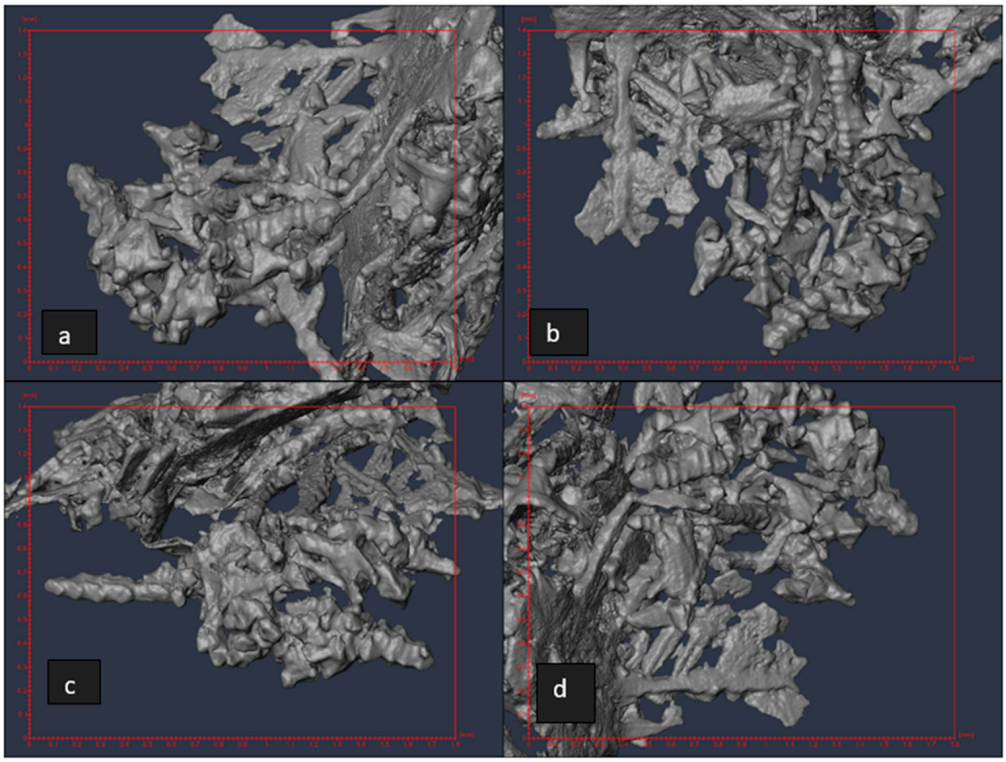

Figure 8. Images illustrating the various crystalline structures within the bulk Ag sample; (**a**) highlights several acicular structures and dendrites, (**b**,**d**) show a herringbone-like twinning texture, and (**c**) shows a single acicular form.

Before discussing the higher resolution images, we point out that further information can be extracted from the examination of bulk crystal assemblages under higher resolution XCT. In fact, both distinct octahedral crystals and triangular platelets can be identified, as shown in Figures 9 and 10, respectively. Although the identification is challenged by some retained lead (see Figure 7b) and the presence of artifacts associated with image processing partially prevents a clear view of the facets of the crystals (Appendix D), there are sufficient examples in our data set [32] to support our conclusions. In particular, it is noted that the octahedral crystals have a size of ~100 μm along the facets, while the triangular platelets are larger, reaching a ~250 μm side length. The triangular platelet also exhibits concavity along their sides, and this is more clearly demonstrated in Figure 5. The implications of these morphological observations are discussed in Section 4.

3.3. Single Ag Crystal Analyzed by High-Resolution XCT

A single crystal with a range of growth textures was chosen for scanning at high resolution using the Zeiss 520 Versa instrument (see Section 2 for details). The results, shown in Figure 11, highlight several growth textures and relationships between grains within the crystal structure.

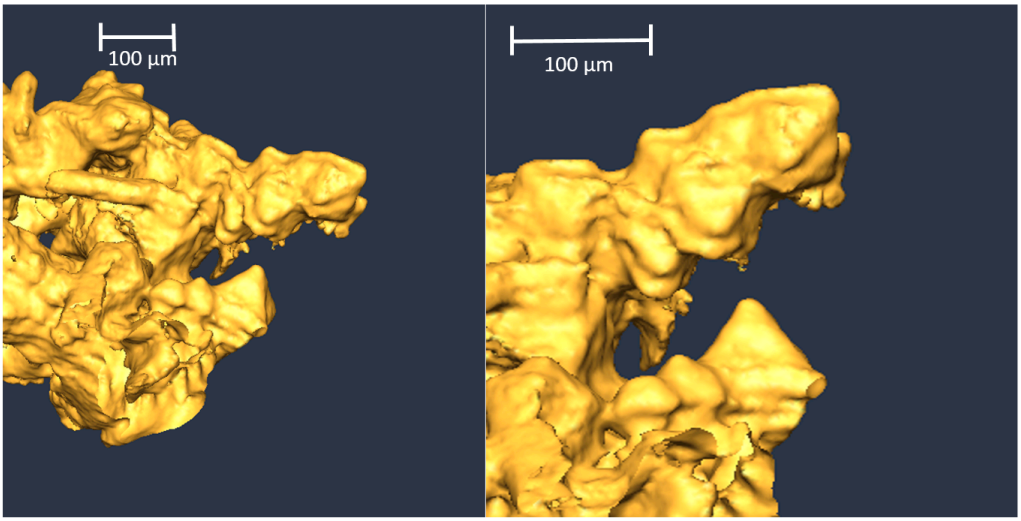

Figure 9. Left: bulk crystal assemblage showing 2 octahedral crystals at base of material. **Right**: the two octahedral crystals as seen from a different orientation. These images are produced by high-resolution XCT experiments.

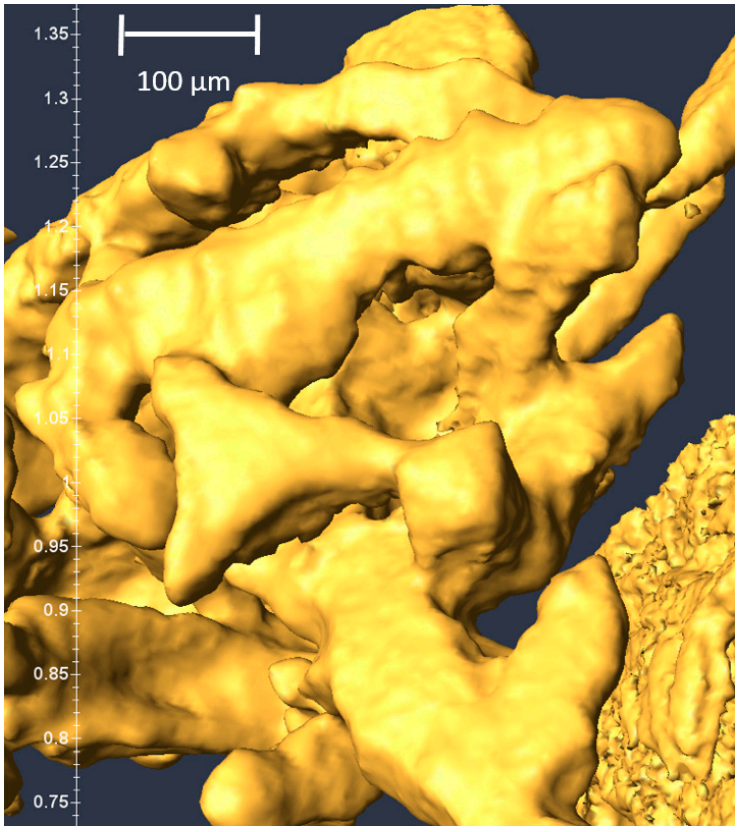

Figure 10. Triangular platelet crystal shown adjacent to octahedron, as observed from high-resolution XCT scans of samples taken from the aggregate shown in Figure 4.

As shown in Figures 5 and 8, a range of grain sizes are present within the crystal structure, with individual component grains ranging from less than 100 µm up to 200 µm in size. These grains exhibit contact twinning and penetrative twinning, yielding a larger crystalline structure. The grains are largely euhedral in form, implying that crystal growth has been under favorable conditions (relatively slow cooling and relatively undisturbed—all experimental runs used in this work have been obtained with similar cooling rates). This results in the well-developed grain forms seen in both Figures 11 and 12, the latter being a

higher magnification of the results shown in Figure 11. The crystal studied here appears to be formed around a grain nucleus, with penetrative twinning occurring near to or at the terminations of the crystal grains. The branches repeat this pattern, with multiple penetrative twins occurring from the terminations of grains, progressively outwards along the branches. There is no consistency regarding the size of the grains growing outwards from the center or regarding the degree of penetration occurring from one neighbor grain to the next, although the final grain in the branch is larger than the preceding ones. The branches are not straight nor of equal length, suggesting that growth can be stochastic.

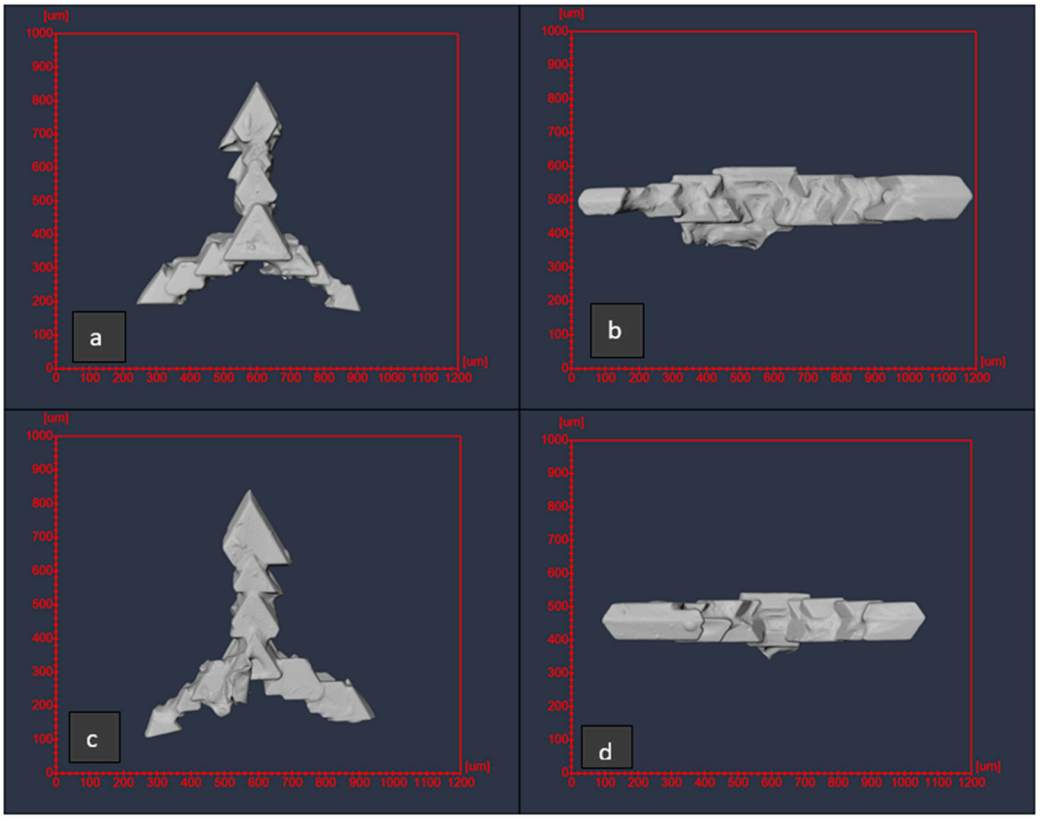

Figure 11. Four different perspectives of a single silver crystal dendrite scanned by the Zeiss Xradia 520 Versa at 4× magnification, with a crystal radius of approximately 400–500 µm. Panel (**a**) and Panel (**c**) are opposing views from the top and bottom, respectively; Panel (**b**) corresponds to the right-hand side of Panel (**a**), and Panel (**d**) corresponds to the right-hand side of Panel (**c**). The literature [33] identifies the top and base of the triangular platelets as {111} planes and the narrow sides between these planes as {100} planes.

Visual analysis of XCT scans such as those shown here suggests that twinning is a dominant behavior within the system investigated, with most grains present exhibiting contact twinning and repetitive penetration twinning as shown in Figure 11. In Figure 12, it appears that there are multiple intergrown grains form the tip of the branch. These penetration twins yield branches with a high aspect ratio. A closer examination of the sample as shown in Figure 12 highlights the degree to which the amount of penetration from one grain to another varies, with one grain almost subsumed into the adjoining crystals as shown in Figure 12c.

Also apparent from the results in Figure 12 is the presence of contact twinning forming each of the individual grains in the branches. In Figure 11, there is evidence of contact twinning (less clear with the lower resolution Nikon scan presented in Figures 7 and 8 above); this is much clearer in Figure 11b,d, where the grain morphology is mirrored across the axis of the structure.

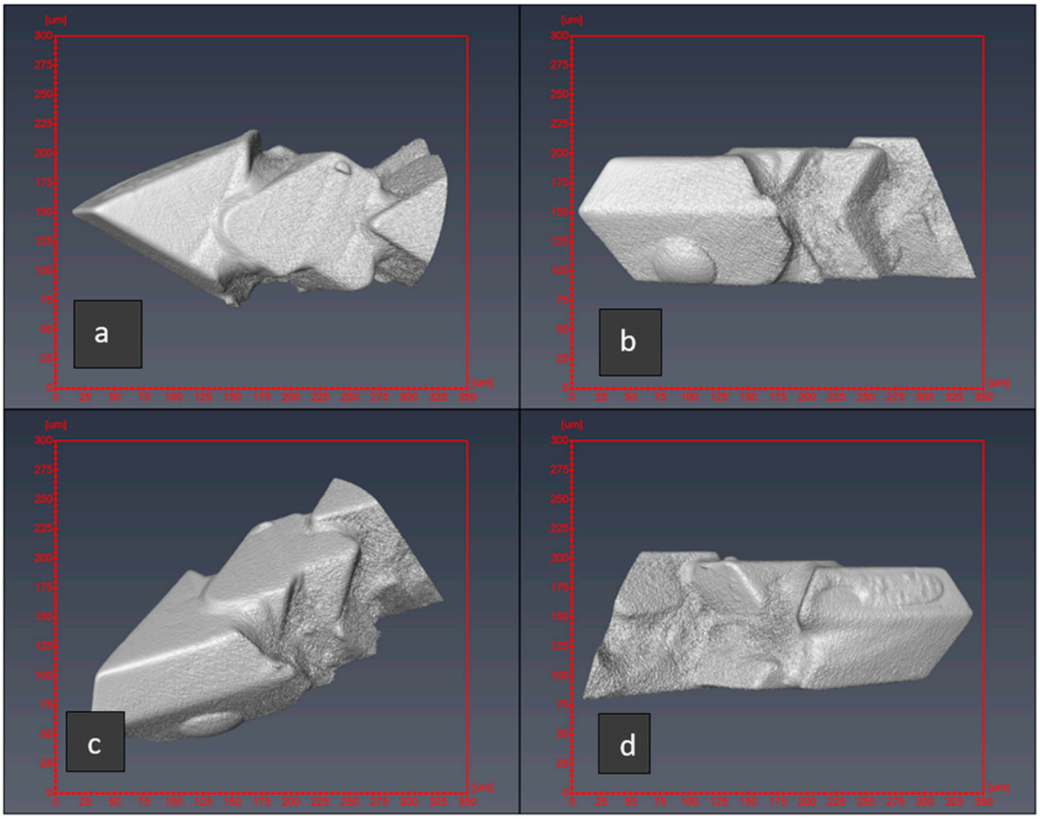

Figure 12. The 40× scan of the end of one of the branches of the silver crystal dendrite as shown in Figure 9. Panel (**a**) is a top-down view of the image, with Panels (**b**,**d**) showing opposite sides of the grains; Panel (**c**) provides a composite reconstruction of Panels (**a**,**b**). The literature [33] identifies the top and base of the triangular platelets as {111} planes and the narrow sides between these planes as {100} planes. This assessment of the crystallographic planes is supported by the measured contact angles between the {100} and {111} planes as 108.8° compared to the expected value of 109.47°.

The results shown in Figures 7 and 8 imply there are a range of different dendrite forms present in the samples produced in this work; the scan of the single crystal dendrite from the Zeiss instrument (Figures 11 and 12) demonstrates the complexity of the structural morphologies present. The bulk sample is composed of multiple crystal structures, each structure being of different dimensions, with different degrees of penetrative twinning with neighboring grains and different twinning textures present. In Section 4, we relate these morphological observations to the mechanism of Ag crystal growth at the commercial conditions considered in this study.

4. Discussion

4.1. Implications for Nucleation and Growth

Imaging analysis conducted across different length scales and shown in the preceding sections provides evidence of dendrites with high aspect ratios and significant interpenetrative twinning showing a wide range of growth timescales. These behaviors can be largely related to the crystalline lattice of Ag. As shown in Figure 13, Ag falls within the isometric crystal system; this can result in Body-Centered Cubic {100} forms, of which none are noted within the sample. Variation in the crystal lattice can lead to an octagonal {111} form, which is indeed noted in Figure 5. This corresponds with silver typically exhibiting Face-Centered Cubic crystal lattice forms [34,35].

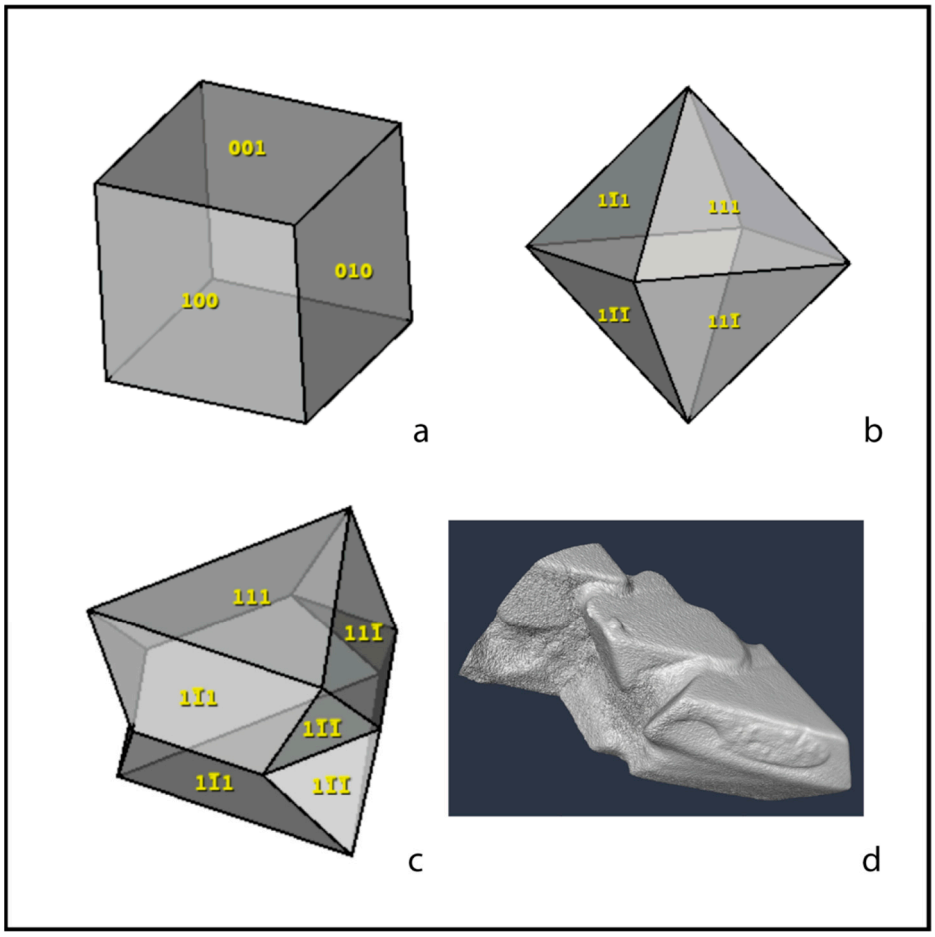

Figure 13. Typical crystal morphologies exhibited by silver [33]: cubic (Body-Centered Cubic), as shown in (**a**); diamond, as in (**b**); contact twins across, as in (**c**) (both of which are Face-Centered Cubic). In panel (**d**), we reproduce the experimental visualization of the tips of Ag crystals obtained in this work, which seems comparable to the contact twinning of panel (**c**).

The imaging of the single crystal dendrite in Figures 11 and 12 shows a prevalence of {111} facets, as discussed in what follows. This corresponds with silver forming a Face-Centered Cubic crystal lattice structure. Many of the grains within the branches of the dendrites exhibit contact twinning along the {111} facet, which is parallel to the horizontal plane of the dendrite. These contact twins point outwards from the center of the dendrite. The branches are composed of multiple grains of this same form and appear as a branch of penetrative twins, implying that at least some of the nucleation events occur on or near the terminations of the formed grains. The grains are not of a uniform size and there is no obvious pattern discernible in terms of their size and their distance from the center of the dendrite. This implies that the grains may have nucleated at different times or had different lengths of time for crystallization to occur, although nothing can be said about the relative timings only based on results obtained from the imaging of the sample. As mentioned above, these observations seem to imply that nucleation is stochastic at the conditions explored herein, which is expected given the degree of cooling, the presence of impurities, and the fact that the commercial system analyzed is bimetallic.

In consideration of the observed Ag crystal morphologies, it must be acknowledged that two distinct influences define the observed outcome. In situations where the timescale is long enough to achieve the thermodynamic conditions corresponding to the minimum surface energy, the crystal morphology will correspond to the Thermodynamic Wulff constructions [36]. In cases where time, system diffusivity, and physical scale lengths obscure the thermodynamic outcome, alternative morphologies, defined by kinetic constraints, will

result in a distinct set of crystal morphologies described by the Kinetic Wulff constructions [36]. Boukouvala and Barmparis examined how fine-scale physical and electronic structure properties control the morphology of nanoparticles [36,37], while Ringe et al. [33] examined the limitations of Thermodynamic Wulff constructions with reference to FCC crystal systems. The analysis provided by Ringe et al. is relevant for our work, as this team examined the morphologies predicted in the kinetic-controlled regime, extended the analysis to twinned nanoparticles, and noted the influence of solution concentration and surface-active species as being significant in determining the final morphology of the grown crystals. It is notable that the crystal morphologies expected under thermodynamic- and kinetic-controlled regimes for FCC materials include octahedra crystals with the triangular platelets being a feature of kinetic-controlled crystals. Boukellal et al. [38] noted that the octahedra morphology encountered in the thermodynamic regime is characterized by rounded contacts between facets with the transition to growth in kinetically controlled regimes. A similar relationship is noted by Xia et al. [39] with truncated octahedra being formed as small seed crystals under thermodynamic control. These are structures observed in the system considered here, as shown in Figure 5 and Figure 9 and Figure 10, respectively; it is worth repeating that the samples considered here were obtained from the commercial-scale cooling of an Ag-Pb molten system, as discussed in the Methods section. It is also worth noting that, in Ringe et al.'s analysis, triangular platelets and columnar needles are only encountered in the FCC system in the kinetically modified regime, which reinforces the reliability of Micro-CT for the characterization of Ag crystals formed from Ag-Pb melts. The earlier reported predominance of the {111} facet in the FCC system is consistent with the octahedra morphology observed in some of our crystals, as well as with structures expected for FCC systems reported by others [40]. It should be noted that predominant growth on the {111} plane will also present crystal morphologies on other planes [36,39,40]; explicitly, the edges of the triangular platelets under kinetic control exposed {100} facets, while the upper and base planes are {111}. All the facets of the octahedra under kinetic control are {111}. It should be noted that the SEM examination of the fine-scale crystal morphologies did not enable determination of the expressed surface growth facet. The relation between observed morphologies and their active growth facets is sourced from the literature [36,39,40], which presents a consistent account.

These results suggest that the {111} facet is the facet of the lowest free energy in our system [41], as indicated by the Bravais theory [15]. The controlled temperature of the melt provides ideal conditions for the euhedral grain forms to develop; larger crystals typically have had the longest period to grow, and the prevalence of twinning resulting in acicular chains and dendrites implies a significant amount of nucleation events on pre-existing grains at different times of cooling. The stirring applied on the cooling alloy mass and localized temperature cycling experienced by crystals could explain these phenomena.

The crystal morphologies discussed above are consistent with crystallization occurring under the kinetically controlled growth regime. While it would be expected that an initial period of constant temperature in the melt would provide conditions that support thermodynamics-controlled morphologies, these are not observed in the samples. It is likely that, in our system, the transition from the crystal nuclei to sharp-faceted octahedra occurs when the crystals are much smaller than those visible in our experiments. This possibility is consistent with observations by Xia et al. [39], who reported a cross-over from truncated octahedrons to Wulff Polyhedrons when crystals contain ~20,000 atoms for silver, which corresponds to a sphere 10 nm in diameter. This size is much smaller than those that can be resolved by the experimental techniques employed here. As crystal growth continues, our results suggest that the process moves into a kinetics-controlled regime, at which point different morphologies occur; initially, the sharp-edged octahedra are observed, and later, as the crystals grow in size, the triangular platelets are observed. This transition is summarized graphically in Figure 14, which presents the morphologies observed in this work under kinetic control and their precursive morphologies under the thermodynamic growth regime, which is consistent with work by other authors [35,39,40]. Because the

system considered comes from cooling of commercial-size samples, and because of the stochasticity of the crystallization events mentioned in the prior parts of the manuscript, it is expected that crystals representing different degrees of growth are present, which explains the structural and size polydispersity observed in our samples. The relative size of the crystals is therefore assumed to be an indirect representation of their age, with smaller crystals representing systems that have had less time to grow than the larger ones.

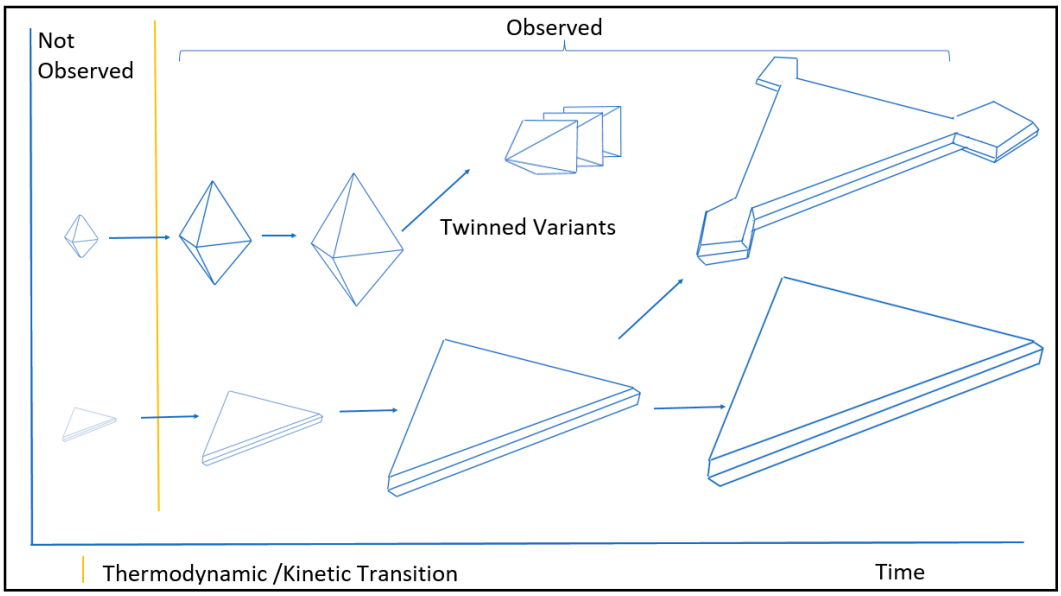

Figure 14. Relationship between observed morphologies and size of Ag crystals. The thermodynamic-controlled morphologies (rounded octahedra and triangular platelets) were not observed here, presumably because of the resolution of the instruments used for characterization, but they are noted as precursors to the kinetic-controlled morphologies that were identified in this work. The generation of twinned variants from the octahedrons and triangular platelets is noted and evidenced by our experimental results.

The scan of the single crystal dendrite (Figure 11) shows that both contact and the penetrative twinning of silver grains occur during the crystallization process in the melt, and the dendrites are growing outwards from the initial nucleus of a crystal. The contact between the grains in the branches appears to be edge-centered, with sequential penetrative crystals growing outwards from the central grain. These are the first examples of silver crystals grown through cooling of a 10% silver–lead melt, partially welded together with a lead matrix, being examined under XCT. This observation is consistent with the discussion above concerning crystal nucleation and growth, in the context of multiple crystallization events taking place at different times during the cooling of commercial-size samples. Our characterization results indicate that there is potential in the use of XCT in the investigation of metallic materials, and comparisons can be drawn with theoretical models of crystal lattices. It is in fact notable that imaging results for crystal morphologies are consistent with the theoretically predicted forms in the FCC system under mostly kinetics-controlled regimes in an environment undergoing solidification from the molten state. The XCT technique as applied herein works most effectively where there is no interference from other materials with similar densities in the samples under investigation.

4.2. Particle Size Distribution

To obtain quantitative information from the XCT scan results, the Avizio software was used to extract dimension and size characterization data for 24 individual crystals [32]. In Appendix A, we report details concerning the procedure implemented. The collective data are presented in Table 2. In the case of the unconsolidated samples obtained from the sample cooling crystallization cycle, the following descriptors were computed:

- Particle size (i.e., radius) distribution;
- Aspect ratio;
- Sphericity;
- Convexity.

Table 2. Shape character summary for 24 crystals using X-ray tomography data from the coherent sample (e.g., materials such as those shown in Figure 4).

	Breadth 3d	Length 3d	Thickness 3d	Width 3d	Sphericity	Shape Factor
	mm	mm	mm	mm		
Mean	0.1738	0.3916	0.0952	0.1195	0.1225	0.1146
Min	0.0577	0.0725	0.0265	0.0318	0.0400	0.0100
Max	0.5041	0.9145	0.2835	0.2686	0.2000	0.3200
Median	0.1486	0.3876	0.0751	0.0973	0.1250	0.1050
Variance	0.0115	0.0460	0.0035	0.0039	0.0021	0.0068
Kurtosis	2.7622	0.4987	2.9990	−0.4043	−0.7674	0.1092
Skewness	1.5050	0.8102	1.5146	0.6427	−0.1067	0.6996

The particle size distribution for one sample is presented in Figure 15. All the particle size data for the three samples were very similar in their mean and standard deviations, and all demonstrated almost identical unimodal distribution curves. Similar behavior was observed in terms of aspect ratio, sphericity, and convexity results as well.

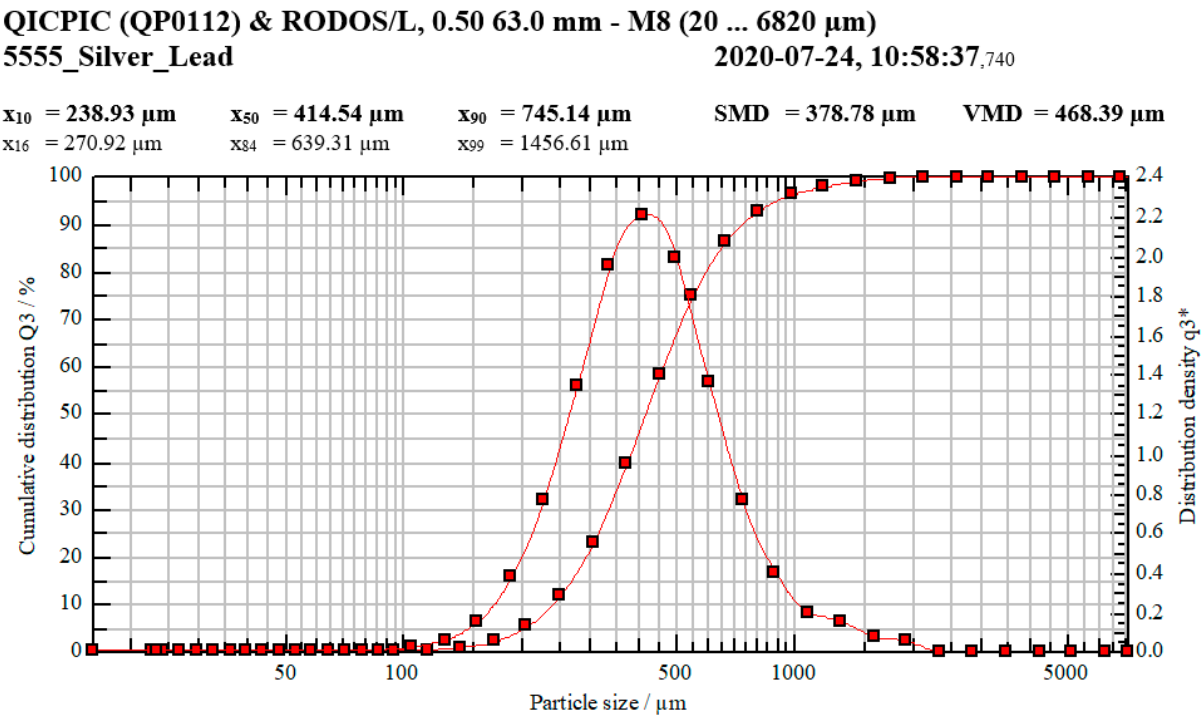

Figure 15. Particle size distribution obtained for sample 1 (see Table 3).

To complement the results obtained for the bulk system, we also characterized the images obtained for Ag crystals in the unconsolidated sample. The results, presented in Table 3, are closely consistent with those shown in Table 2. The similarity in particle size between the three samples is likely due to the common thermal cycle they experienced, having been recovered from a single cooling and crystallization cycle.

Table 3. Unconsolidated sample size and shape results.

Sample No	PSD Mean µm	PSD SD µm	Aspect Ratio Mean	Aspect Ratio SD	Convexity Mean	Convexity SD	Sphericity Mean	Sphericity SD
1	414.54	224.77	0.6557	0.1238	0.7910	0.0565	0.6847	0.0916
2	411.31	217.75	0.6585	0.1206	0.7926	0.0544	0.6848	0.0922
3	421.76	256.06	0.6618	0.1206	0.7933	0.0560	0.6807	0.0941
Mean	415.87	232.86	0.6587	0.1217	0.7923	0.0556	0.6834	0.0926

Although the XCT data allow us to visualize the structure of the Ag crystals at high resolution, it is only possible to use that technique to assess a few of the crystals present within the samples produced. To assess whether the XCT scan results are representative of the produced Ag samples, we compare them to particle size distributions obtained via laser sizing. The procedures implemented to extract sizing data from the laser experiments are presented in Appendices A and B. Despite the differences in the measured size parameters and shape descriptors between the 3D processed data acquired from X-ray tomography and those from the laser sizing, comparison is possible in terms of the results for particle mean size and standard deviation (SD) and aspect ratio mean and SD, obtained from XCT and laser sizing, as compared in Table 4. The mean particle size obtained from the two methods differs by only 9%, and the aspect ratios, although differing by 33%, have means that are close to each other. The laser sizing mean is within 0.74 standard deviations from the tomography mean and the tomography mean is within 1.34 standard deviations from the laser mean. The conformance of size and shape parameter data demonstrates a morphologically consistent product, and the close correspondence between particle size distribution established by XCT and laser gives confidence in the ability of X-ray tomography to determine mean particle sizes in a coherent crystal mass. It should be further emphasized that the two data sets were prepared by different researchers, and they were analyzed at different facilities at different times.

Table 4. Particle size and aspect ratio for 3D tomography of consolidated particles versus laser sizing results of unconsolidated crystals.

3D Tomography	3D Tomography	Laser	Laser
X mean µm	X SD µm	X mean µm	X SD µm
454.65	116.19	415.87	232.86
Aspect Ratio Mean	Aspect Ratio SD	Aspect Ratio Mean	Aspect Ratio SD
0.4953	0.2216	0.6587	0.1217

5. Conclusions

Complex micron-size silver crystal structures, composed of multiple intertwined grains, were found to form within a cooling lead–silver melt from commercial conditions undergoing convection. The characterization results presented herein are consistent with morphologies reported by other researchers [33], where crystal growth was predominantly orientated in the {111} plane for FCC metals. Our results would indicate that this behavior occurs even at commercially relevant conditions from a cooling Ag-Pb molten system.

The observation above is consistent with findings reported for FCC metals deposited by electrolytic means from aqueous solutions, systems on which most of the previous experimental characterization has been reported in the literature. For completeness, it should be noted that predominant growth on the {111} plane allows for the presentation of crystal morphologies on other planes [36,39,40] as well; specifically, our results are consistent with the edges of the triangular platelets representing {100} planes under kinetic growth control, while the upper and base planes are {111}. All the facets of the octahedra under kinetic control expose {111} planes.

In addition, our results show a variety of crystal sizes and shapes that are found within the bulk sample, with most crystalline grains being subhedral to euhedral in shape and ranging from below 100 μm up to 200 μm in size, with the larger crystal structures up to 1000 μm in size. Analysis of the crystal aggregate in 3D as enabled by XCT results shows that both octahedral crystals and larger triangular platelets are formed, although the presence of residual artifacts prevents the facets of the crystals from being resolved clearly. In our interpretation, the crystal size is used as a surrogate measurement of the time the crystals have had to grow, with smaller crystals representing materials that have had less opportunity to grow compared to larger crystals. Hence, considering the fact that the predominant morphology of the silver crystals changes with crystal size, our results suggest a transition in the growth mechanism with time (and therefore with crystal size). Our interpretation is consistent with expectations for crystals of FCC systems grown under thermodynamics- and kinetics-controlled regimes. It is possible that the first nuclei form under thermodynamic-controlled conditions, but these crystals (not observed because they are too small compared to the resolution of our XCT instrumentation) rapidly transition into the kinetically controlled growth mechanism. This possibility is consistent with the literature observations for other FCC materials. System conditions that could affect the morphology of the Ag crystals could include the cooling rate and the presence of impurities. These two possibilities are difficult to probe for the system considered here because of the commercial size of the sample being used for the experiments.

The results presented here demonstrate that XCT has potential as a method to investigate the morphologies of metallic crystals and their composing grains in bulk and at different scales, formed from the cooling of a silver–lead melt, provided that the experiments are conducted at conditions at which attenuation is managed and mitigated. In our measurements, small crystals were used, and the technical process was optimized to remove the liquid lead phase and impregnate the open pore spaces between the silver crystals with an acrylic resin under vacuum.

When these innovations are implemented, low-resolution X-ray scans of bulk crystals in the XCT configuration are found to be capable of partially resolving individual grain morphologies, though there remains room for improvement in fully resolving the facets of grains and crystals and minimizing artifacts. The higher resolution scans can detail and characterize individual crystal structures. The analysis of the experimental scans at different scales obtained herein documents a pronounced twinning behavior exhibited across the samples, demonstrating the utility of the technique. Our results suggest that grain growth is accompanied by twinning on the {111} plane, resulting in complex triangular-faced grains.

Although optical microscopy and SEM can provide clear images, the XCT results provide an understanding of the 3D internal structure, including, for example, the pore structure, of the aggregate crystal mass that could not be achieved solely from examination of the surface of the unconsolidated crystals. However, there remains room for improvement in resolving the facets of individual silver crystals and grains at this scale, which would allow for a quantitative assessment of pore structure, for example, to be undertaken.

Supporting the potential of the experimental approach discussed, the particle size distribution obtained by the analysis of the X-ray tomography results was found to be consistent with laser sizing analysis conducted via a double-blind study. This strongly suggests that the XCT results are representative of the samples produced and that X-ray tomography can potentially be applied to quantify crystal assembly in lead–silver systems, where attenuation related to the high atomic mass of the specimen material presents significant technical challenges, when artifacts can be suppressed, and the details were resolved clearly. When these issues are mitigated for, this technique could allow the community to gain an additional quantitative understanding of crystal growth, grain behaviors, and crystalline lattices under specific conditions (e.g., in the presence of impurities), allowing for different operating conditions to be investigated.

Author Contributions: S.K. was responsible for conceptualization, methodology (samples acquisition), data curation, formal analysis, and writing the original draft; A.N.-M. was responsible for methodology and data acquisition (XCT); D.R. collected some of the data presented; A.S. was responsible for project management, project administration, and interpretation of the results. All authors were responsible for reviewing and editing the original draft. All authors have read and agreed to the published version of the manuscript.

Funding: Funding for this manuscript was provided, in part, by Glencore. AS acknowledges financial support by the Asahi Glass Co. group via the Asahi Glass Chair of Chemical Engineering, as well as by the School of Chemical, Biological and Materials Engineering at the University of Oklahoma.

Data Availability Statement: Data are contained within the article and Appendices A–D. Additional data can be requested via email from Steven King.

Acknowledgments: Part of the characterization studies were conducted as part of an MSc dissertation within the Department of Chemical Engineering at University College London.

Conflicts of Interest: The authors declare no conflicts of interest.

Appendix A. Shape Characterization for Ag Crystals

The dimension and shape parameters are defined as follows.

Feret Diameter

The distance of two tangents to the particle in a well-defined orientation. These dimensions could be equivalently measured by application of a slide gauge to the particle. Measurement of the Feret diameters over a range of angles enables the selection of maximum and minimum values, as shown schematically in Figure A1 (Sympatic 2021) [42].

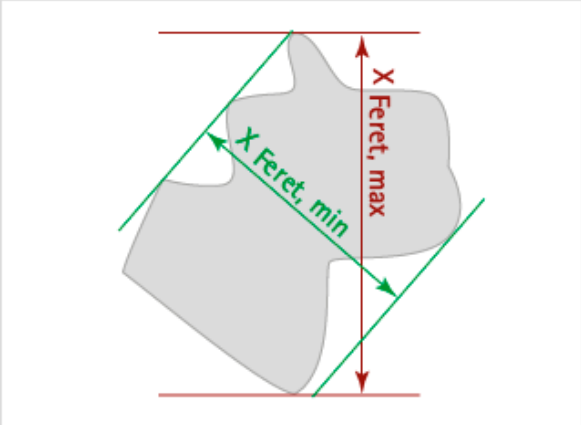

Figure A1. Section showing Feret max and min diameters (Sympatec 2021).

Length: The maximum Feret diameter.

Width: The minimum Feret diameter

Breadth: The largest distance between 2 parallel lines contacting the object at tangents, without intersecting the object, and lying in a plane orthogonal to the maximum Feret diameter. The above definition is also termed the max Feret 90°.

Thickness: The largest segment that touches the object by its end points and lying in a plane orthogonal to the maximum Feret diameter and orthogonal to the breadth diameter.

Sphericity: The sphericity of a particle is defined as the ratio of the surface area of a sphere of the same volume as the particle to the measured actual surface area of the particle. The sphericity of a sphere equals one, while all other shapes have a sphericity of less than one.

$$\text{Sphericity } (\psi) = \pi^{1/3} \text{x } (6V)^{2/3}/A$$

Shape Factor: Another particle index based on the area-to-volume ratio:

$$\text{Shape factor} = A^3/36\pi V^2$$

Shape factor and sphericity are related as:

$$\text{Sphericity } (\psi) = (1/\text{shape factor})^{1/3}$$

In the above set of shape parameter definitions, length, breadth, and thickness define the smallest rectangular prism that the particle could be packed into. The mutual orthogonality of the length, breadth, and thickness measurements defines them as the major and minor (2) diameters of a triaxial ellipsoid.

Laser Sizing Dimension and Shape Characterization

In the case of dynamic laser size and shape characterization, the data set consists of a series of projected areas of the particle in random orientations. The dimensional parameters measured with laser sizing are consistent with those utilized with optical microscopy [42,43] and are detailed below.

Breadth: The minimal distance between 2 parallel lines tangential to the projected outline of the particle when placed in the most stable position; resting on a flat surface under observation.

Length: Distance between 2 tangents to the projected outline of the particle drawn perpendicularly to the tangents defining the breadth.

Thickness: Distance between 2 planes tangential to the surface of the particle and parallel to the plane of the projected image.

In this definition, the mutual orthogonality of the breadth, length, and thickness measurements establishes them as equivalent to those obtained with X-ray tomography and provides the ability to examine the particle dimensions from all orientations.

Diameter of a Circle of Equal Projection Area/EQPC: This is the diameter of a circle that has the same area (A) as the projection area of the particle (see Figure A2).

$$X_{EQPC} = 2\sqrt{A/\pi}$$

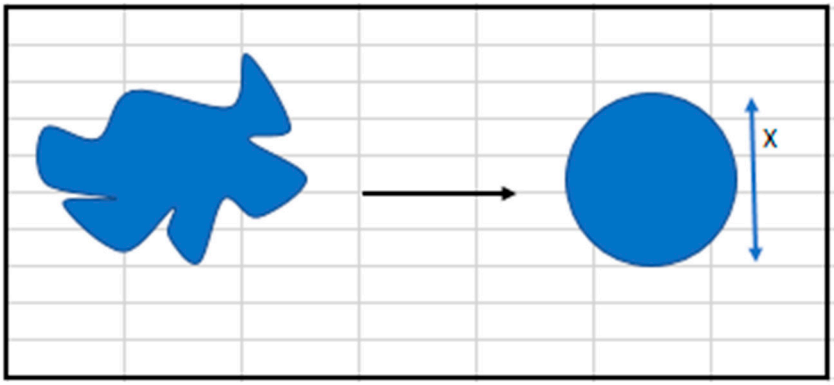

Figure A2. Circle of diameter X of same area as projected shape.

Aspect Ratio: The ratio of the minimum to the maximum Feret diameters:

$$\text{Aspect ratio} = X_{\text{Feret Min}}/X_{\text{Feret Max}}$$

In comparison to the X-ray tomography 3D definitions, this is equivalent to width/length, emphasizing that these lengths as measured may not be orthogonal.

Sphericity: The sphericity S (see Figure A3) is the ratio of the perimeter of the equivalent circle P_{EQPC} to the real perimeter P_{REAL}.

Convexity: The convexity (see Figure A4) is the ratio of the projection area itself (A) and the area of the convex hull (A + B) (Sympatec 2021) [42].

In dynamic laser sizing (as distinct from static particle microscopy), the "snapshot" images will define a large data set of random projected particle cross-sections, and as such this will enable a valid comparison to the size and shape parameters determined using X-ray tomography. The particle characteristic dimensions are presented in Figure A5. The laser

sizing assessment was conducted on three 20 g samples of unconsolidated silver crystals. The dynamic imaging captured the dispersed crystals' silhouettes at random orientations using the PICTOS disperser system, with image processing using the QICPIC software.

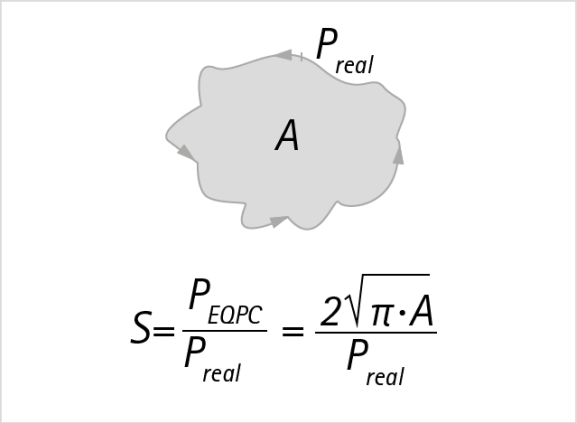

Figure A3. Definition of particle sphericity (Sympatec 2021) [42].

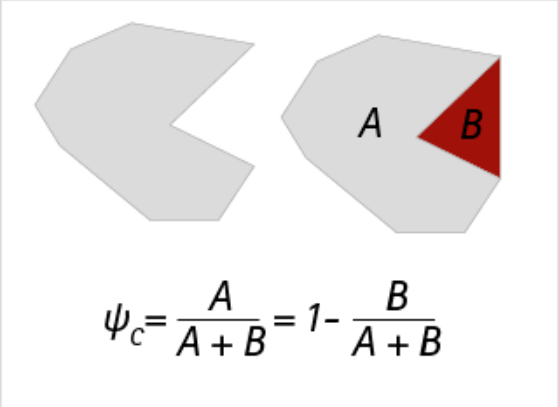

Figure A4. Definition of particle convexity (Sympatec 2021) [42].

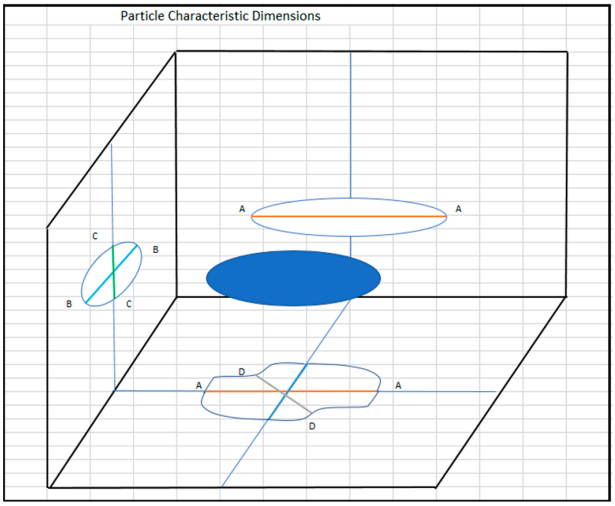

Figure A5. A representative particle is shown in blue. Its appearance is projected on three planes, where the particle characteristic dimensions can be extracted. These are: A-A = length (orange), B-B = breadth (blue), C-C = thickness (green), D-D = width (grey).

Appendix B. Size and Shape Characterization from Laser Experiments

Equivalent Diameter

If the dynamic laser sizing is considered to have an equal opportunity to obtain particle silhouettes from any orientation, this will mean that with reference to Figure A5, the mean silhouette area will be defined by:

$$A_{mean} = \pi/3(AB/4 + AC/4 + BC/4)$$

Thus, $X_{EQPC} = 2\sqrt{A\ mean/\pi}$.

Aspect ratio

The aspect ratio is generated for the laser sizing and defined as Feret min/Feret max, as the 2 lengths must be in an orthogonal plane, and the best representation of the aspect ratio from X-ray tomography data may be equivalently generated from the X-ray tomography data as the ratio of breadth/length.

Sphericity

The definition of sphericity based on 3D data is different to that based on 2D silhouettes. Although both functions equal 1 for spheres, the 3D sphericity is a ratio of length squared while the laser sizing sphericity is a ratio of lengths, and thus a similar population of particles will have different sphericity values for each method. To attempt a comparison would require assumptions about the aspect ratios of the particles that could not be supported by evidence. As such, sphericity is not compared between the 2 data sets.

Shape Factor

As shape factor is functionally related to sphericity, it will not be examined.

Concavity

As concavity is only presented in the laser sizing data, the opportunity to compare to a 3D shape parameter does not exist.

Appendix C. SEM Power Spectrum for Ag Crystals

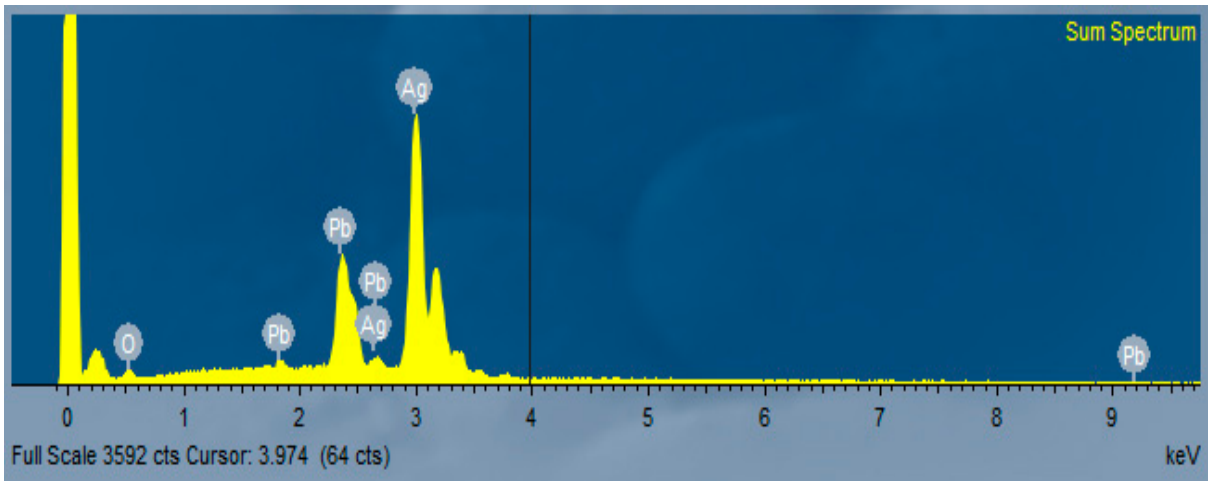

Figure A6. The qualitative power spectrum for Ag crystals demonstrates Pb as the primary impurity with oxygen also being identified.

Appendix D. Nikon Greyscale Images of Silver Crystal Assemblages

The greyscale images of crystal aggregates as obtained with the Nikon imaging system (Figures A7 and A8) demonstrate the presence of some artifacts and also traces of retained lead in some of the image field. Although the aggregate images do not permit the resolution of crystal facets, different crystal morphologies can be identified from the visual analysis of these images.

The greyscale images of individual crystals obtained with the Zeiss Xradia 520 Versa imaging system (Figures A9 and A10) demonstrate fewer artifacts compared to results from the Nikon system, thus allowing for the improved identification of morphologies.

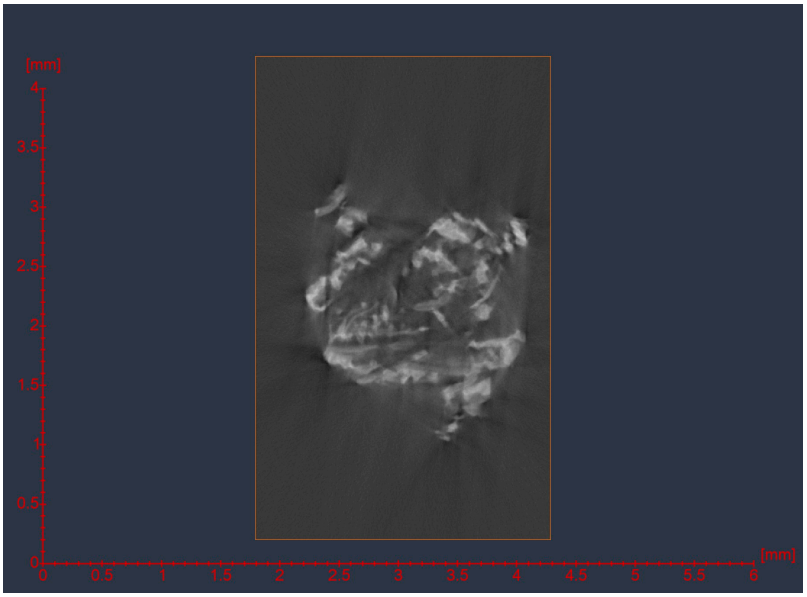

Figure A7. Nikon XT H 225 greyscale cross-section. The metallic crystals are in high contrast (white) with respect to the rest of the volume.

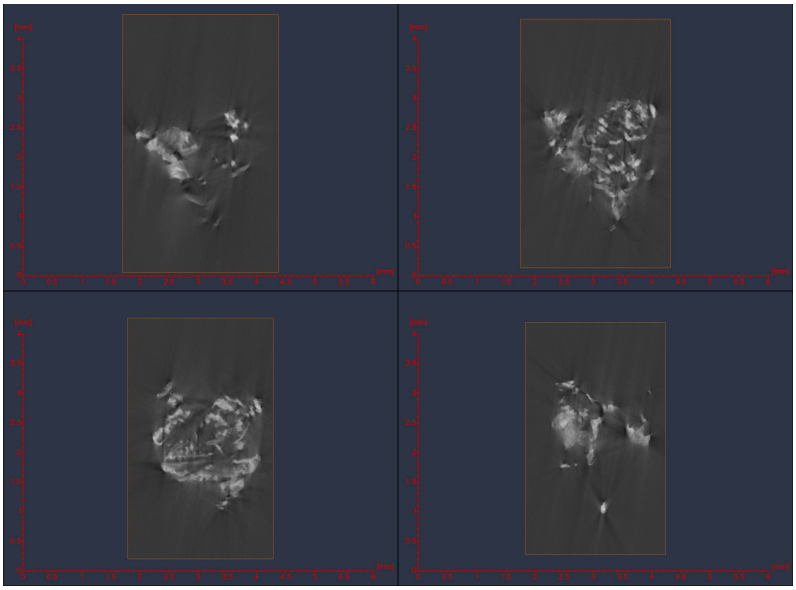

Figure A8. Nikon XT H 225 greyscale cross-section, 4x panel. The metallic crystals are in high contrast (white) with respect to the rest of the volume.

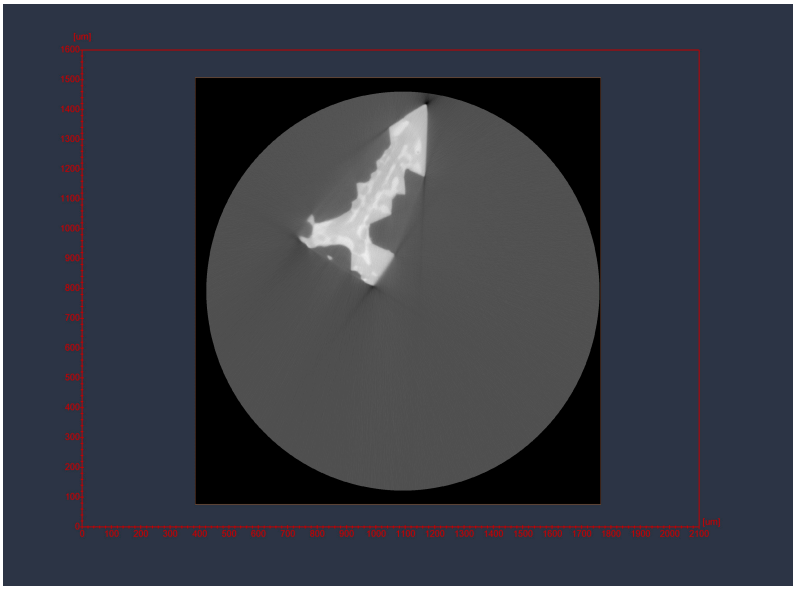

Figure A9. Zeiss Xradia 520 Versa greyscale cross-section with 4x objective magnification. The silver crystal is in high contrast (white) with respect to the remainder of the volume.

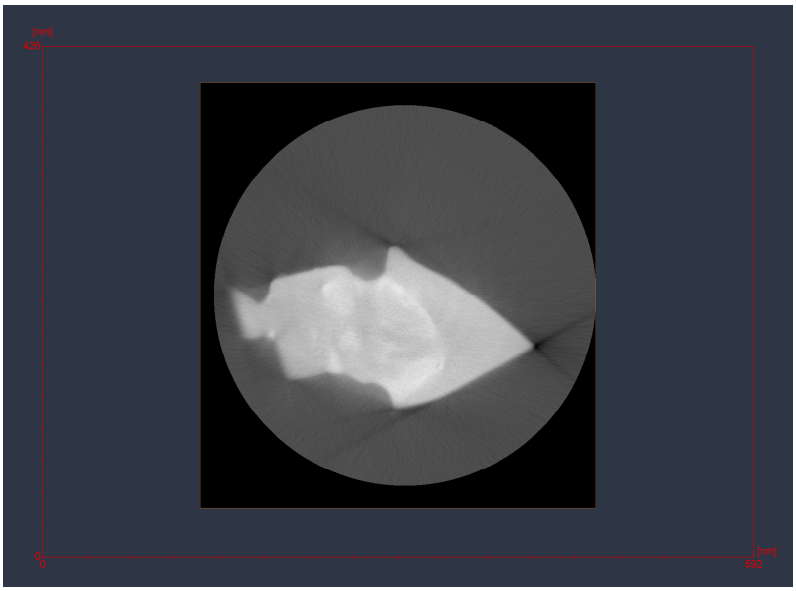

Figure A10. Zeiss Xradia 520 Versa greyscale cross-section, 20× magnification. The portion of the silver crystal scanned is in high contrast (white) with respect to the remainder of the volume.

References

1. Butterman, W.; Hilliard, H. *Mineral Comodity Profiles: Silver*; US Geological Survey Publication: Reston, VA, USA, 2005. [CrossRef]
2. Butts, A.; Coxe, C. *Silver Economics Metallurgy and Use*; Van Nostrand: New York, NY, USA, 1967.
3. Jezowska-Trzebiatowska, B.; Stanisław, K.; Teofil, M. *The Rare Elements: Occurrence and Technology*; PWN: Warszawa, Poland, 1990.
4. Bornet, R. Le-Comptoir-Geologique. Available online: http://www.le-comptoir-geologique.com (accessed on 20 May 2022).
5. Geology.Com Silver Page. Available online: https://geology.com/minerals/silver.shtml (accessed on 20 May 2022).
6. Murphy, C.J.; Jana, N. Controlling the Aspect Ratio of Inorganic Nanorods and Nanowires. *Adv. Mater.* **2002**, *14*, 80–82. [CrossRef]
7. Dvolaitzky, M.; Ober, R.; Taupin, C.; Anthore, R.; Auvray, X.; Petitas, C.; Williams, C. Silver Chloride Microcrystals Suspensions in Microemulsions Media. *J. Dispers. Sci. Technol.* **1983**, *4*, 29–45. [CrossRef]
8. Fan, L.; Guo, R. Growth of Dendritic Silver Crystals in CTAB/SDBS mixed surfactant solutions. *J. Cryst. Growth Des.* **2008**, *8*, 2150–2156. [CrossRef]
9. Herriman, R.W. Crystal Growth During the Formation of a Silver-Bromide Dispersion in Gelatin. *J. Photogr. Sci.* **1964**, *12*, 121–133. [CrossRef]

10. Lui, H.; Wang, H.; Guo, R.; Cao, X.; Zhao, J.; Luo, Y.; Shen, M.; Zhang, G.; Shi, X. Size Controlled Synthesis of Dendrimer-Stabilized Silver Nanoparticles for X-ray Computed Tomography Imaging Applications. *Polym. Chem.* **2010**, *1*, 1677–1683. [CrossRef]
11. Smith, C.T.G.; Mills, C.A.; Pani, S.; Rhodes, R.; Bailey, J.J.; Cooper, S.J.; Pathan, T.S.; Stolojan, V.; Brett, D.J.L.; Shearing, P.R.; et al. X-ray micro-computed tomography as a non-destructive tool for imaging the uptake of metal nanoparticles by graphene-based 3D carbon structures. *Nanoscale* **2019**, *11*, 14734–14741. [CrossRef] [PubMed]
12. You, H.; Chen, F.; Yang, S.; Yang, Z.; Ding, B.; Liang, S.; Song, X. Size effect on nanoparticle-mediated silver crystal growth. *Cryst. Growth Des.* **2011**, *11*, 5449–5456. [CrossRef]
13. Pangarov, N.A. The Crystal Orientation of Electrodeposited Metals. *Electrochim. Acta* **1962**, *9*, 139–146. [CrossRef]
14. Nikolić, N.D.; Vesna, M.M.; Avramović, L. Correlation of Morphology and Crystal Structure of Metal Powders Produced by Electrolysis Processes. *Metals* **2021**, *11*, 859. [CrossRef]
15. Rosenberg, A.; Tiller, W.A. The Relationship between Growth Forms and the Preferred Direction of Growth. *Acta Metall.* **1957**, *5*, 565–573. [CrossRef]
16. Chattopadhay, C.; Sangal, S.; Mondal, K. A relook at the preferred growth direction of the solid-liquid interface during solidification of pure metals. *Acta Mater.* **2010**, *58*, 5342–5353. [CrossRef]
17. Mori, Y.; Harad, H.; Yokokawa, T.; Kobayashi, T.; Suzuki, S. Directionally-Solidified Dendrite Morphology with eight secondary arms in an FCC ordered phase alloy. *J. Cryst. Growth* **2018**, *500*, 15–22. [CrossRef]
18. Tiller, W.A. Preferred growth direction in metals. *JOM* **1957**, *9*, 850–855. [CrossRef]
19. Hoyt, J.J.; Asta, M.; Haxhimali, T.; Karma, A.; Napolitano, R.E.; Trivedi, R.; Laird, B.B.; Morris, J.R. Crystal-Melt Interfaces and Solidification Morphologies in Metals and Alloys. *MRS Bull.* **2004**, *29*, 935–939. [CrossRef]
20. Henry, S.; Minghetti, T.; Rappaz, M. Dendrite Growth Morphologies in Aluminium Alloys. *Acta Mater.* **1998**, *46*, 6431–6443. [CrossRef]
21. Soper, A.; McCafferty, K.; Erb, U. The Effects of Temperature and Bismuth Impurities on Preferred Orientations of Copper and Silver on Amorphous Silica. *Phys. Status Solidi A Appl. Res.* **1993**, *139*, 371–377. [CrossRef]
22. Butzloff, P.R. Micro-CT imaging of denatured chitin by silver to explore honey bee and insect pathologies. *PLoS ONE* **2011**, *6*, e27448. [CrossRef]
23. Zou, J.; Hannula, M.; Misra, S.; Feng, H.; Labrador, R.H.; Aula, A.S.; Hyttinen, J.; Pyykkö, I. Micro CT Evaluation of Silver Nanoparticles in the Middle and Inner Ear of Rat and Transportation Pathway after Transtympanic injection. *J. Nanobiotechnology* **2015**, *13*, 5. [CrossRef]
24. Lin, W.; Zhou, B.; Liu, Y.; Guo, X.; Zheng, T.; Zhong, Y.; Zhang, L.; Zhang, Q.; Wang, Q. Dendrite Morphology in Al-20 wt%Cu Hypoeutectic Alloys in 24 T High Magnetic Field Quantified by Ex-Situ X-Ray Tomography. *J. Alloys Compd.* **2022**, *918*, 165679. [CrossRef]
25. Mayorga-González, R.; Rivera-Torrente, M.; Nikolopoulos, N.; Bossers, K.W.; Valadian, R.; Yus, J.; Seoane, B.; Weckhuysen, B.M.; Meirer, F. Visualizing Defects and Pore Connectivity Within Metal-Organic Frameworks by X-Ray Transmission Tomography. *Chem. Sci.* **2021**, *12*, 8458–8467. [CrossRef]
26. Østergaard, M.B.; Cai, B.; Petersen, R.R.; König, J.; Lee, P.D.; Yue, Y. Impact of pore structure on the thermal conductivity of glass foams. *Mater. Lett.* **2019**, *250*, 72–74. [CrossRef]
27. Godinho, J.; Gerke, K.; Stack, A.; Lee, P.D. The dynamic nature of crystal growth in pores. *Sci. Rep.* **2016**, *6*, 33086. [CrossRef] [PubMed]
28. Alkemper, J.; Voorhees, P.W. Quantitative Serial Sectioning Analysis. *J. Microsc.* **2001**, *201*, 388–394. [CrossRef] [PubMed]
29. Karakaya, I.; Thompson, W.T. The Ag-Pb (Silver-Lead) system. *Bull. Alloy Phase Diagr.* **1987**, *8*, 326–334. [CrossRef]
30. NIST: Phase Diagram and Computational Thermodynamics Ag-Pb System. Available online: https://www.metallurgy.nist.gov/phase/solder/agpb.html (accessed on 20 May 2022).
31. Avizo Software User's Guide 2019 Thermo-Fisher Scientific. Available online: https://assets.thermofisher.com/TFS-Assets/MSD/Product-Guides/users-guide-avizo-software-2019.pdf (accessed on 21 September 2020).
32. Rajoo, D.L. Characterization of Metallic Sample Properties from a Multi-Stage Extractive Metallurgical Process. Master's Dissertation, University College London, London, UK, 2019.
33. Ringe, E.; Van Duyne, R.P.; Marks, L.D. Kinetic and Thermodynamic Modified Wulff Constructions for Twinned Nanoparticles. *J. Phys. Chem. C* **2013**, *117*, 15859–15870. [CrossRef]
34. Goldschmidt, V. *Atlas Der Krystallformen*; Winters: Stanford, CA, USA, 1913.
35. Vegard, L. The structure of silver crystals. *Lond. Edinb. Dublin Philos. Mag. J. Sci.* **1916**, *31*, 83–87. [CrossRef]
36. Christina, B.; Daniel, J.; Ringe, E. Approaches to Modelling the Shape of Nanocrystals. *Nano Converg.* **2021**, *8*, 26. [CrossRef]
37. Barmparis, G.D.; Lodziana, Z.; Lopez, N.; Remediakis, I.N. Nanoparticle Shapes by Using Wulff Constructions and First-Principles Calculations. *Beilstein J. Nanotechnol.* **2015**, *6*, 361–368. [CrossRef]
38. Boukellal, A.K.; Elvalli, A.K.S.; Debierre, J.-M. Equilibrium and Growth Facetted Shapes in Isothermal Solidification of Silicon: 3D Phase-Field Simulations. *J. Cryst. Growth* **2019**, *522*, 37–44. [CrossRef]
39. Xia, Y.; Xiong, Y.; Lim, B.; Skrabalak, S.E. Shape-Controlled Synthesis of Metal Nanocrystals: Simple Chemistry Meets Complex Physics? *Angew. Chem. Int. Ed.* **2009**, *48*, 60–103. [CrossRef]
40. Marks, L.D.; Peng, L. Nanoparticle Shape, Thermodynamics and Kinetics. *J. Phys. Condens. Matter* **2016**, *28*, 053001. [CrossRef] [PubMed]

41. Lončarić, I.; Despoja, V. Benchmarking Van der Waals Functionals with noncontact RPA Calculations on Graphene-Ag(111). *Phys. Rev. B-Condens. Matter Mater. Phys.* **2014**, *90*, 075414. [CrossRef]
42. Sympatec Particle Measurement GLOSSARY 2021. Available online: https://www.sympatec.com/en/particle-measurement/glossary/ (accessed on 20 September 2023).
43. Heywood, H. Numerical Definitions of Particle Size and Shape. *J. Soc. Chem. Ind.* **1937**, *56*, 149–154. [CrossRef]